The Na^+-pumping mechanism driven by redox reactions in the NADH-quinone oxidoreductase from *Vibrio cholerae* relies on dynamic conformational changes

Moe Ishikawa-Fukuda[1,2]†, Takehito Seki[3,4]†, Jun-ichi Kishikawa[5,6]*, Takahiro Masuya[1], Kei-ichi Okazaki[3,4], Takayuki Kato[6], Blanca Barquera[2], Hideto Miyoshi[1], and Masatoshi Murai[1]*

[1]Division of Applied Life Sciences, Graduate School of Agriculture, Kyoto University, Kyoto, Kyoto 606-8502, Japan, [2] Center for Biotechnology and Interdisciplinary Studies, Rensselaer Polytechnic Institute, Troy, NY 12180, United States, [3]Research Center for Computational Science, Institute for Molecular Science, National Institutes of Natural Sciences, Okazaki, Aichi 444-8585, Japan, [4]Graduate Institute for Advanced Studies, SOKENDAI, Okazaki, Aichi 444-8585, Japan, [5]Faculty of Applied Biology, Kyoto Institute of Technology, Kyoto, Kyoto 606-8585, Japan, [6] Institute for Protein Research, The University of Osaka, Suita, Osaka565-0871, Japan.

†M.I-F. and T.S. contributed equally to this work.

*To whom correspondence should be addressed:

- Masatoshi Murai, Division of Applied Life Sciences, Graduate School of Agriculture, Kyoto University, Japan (murai.masatoshi.5s@kyoto-u.ac.jp),
- Jun-ichi Kishikawa, Faculty of Applied Biology, Kyoto Institute of Technology, Japan (kishijun@kit.ac.jp).

SUMMARY

The Na^+-pumping NADH-quinone oxidoreductase (Na^+-NQR) is a key respiratory enzyme in many marine and pathogenic bacteria that couples electron transfer to Na^+-pumping across the membrane. Earlier X-ray and cryo-EM structures of Na^+-NQR from *Vibrio cholerae* suggested that the subunits harboring redox cofactors undergo conformational changes during catalytic turnover. However, these proposed rearrangements have not yet been confirmed. Here, we have identified at least five distinct conformational states of Na^+-NQR using: mutants that lack specific cofactors, specific inhibitors or low-sodium conditions. Molecular dynamics simulations based on these structural insights indicate that 2Fe-2S reduction in NqrD/E plays a crucial role in triggering Na^+ translocation by driving structural rearrangements in the NqrD/E subunits, which subsequently influence NqrC and NqrF positioning. This study provides the first structural insights into the mechanism of Na^+ translocation coupled to electron transfer in Na^+-NQR.

INTRODUCTION

The Na^+-pumping NADH-quinone oxidoreductase (Na^+-NQR) is the first enzyme in the respiratory chain of numerous marine and pathogenic bacteria, including *Vibrio cholerae*, *Neisseria gonorrhoeae,* and *Haemophilus influenzae*. Na^+-NQR catalyzes the transfer of electrons from NADH to quinone, coupled to the translocation of Na^+, generating an electrochemical Na^+ gradient across the inner membrane. This gradient powers essential energy-dependent processes such as ATP synthesis, rotation of the flagellar motor, transport of nutrients, and operation of multi-drug transporters[1–3]. As originally revealed by biochemical and biophysical studies, Na^+-NQR is an integral membrane complex composed of six subunits (NqrA-F) encoded by the *nqr* operon, with five spectroscopically visible redox cofactors (FAD, 2Fe-2S, 2FMNs, and riboflavin) and a total molecular mass or approximately 200 kDa Na^+-NQR is exclusively found in prokaryotes and is structurally unrelated to the mitochondrial H^+-pumping NADH-quinone oxidoreductase (respiratory complex I), making it a promising target for highly selective antibiotics[3,4].

X-ray crystallographic[5,6] and single-particle cryo-EM analyses[6,7] have revealed the entire architecture of Na^+-NQR (Fig. 1a). The cytoplasmic domain of the NqrF subunit includes a Rossmann nucleotide binding motif, where NADH binds, and contains one non-covalently bound FAD (FAD^{NqrF}) that is the initial acceptor of electrons, and one 2Fe-2S cluster ($2Fe\text{-}2S^{NqrF}$)[8,9]. The membrane-embedded NqrD and NqrE subunits form an inverted repeat structure that coordinates a second 2Fe-2S ($2Fe\text{-}2S^{NqrD/E}$) [2,10–12], originally assigned as a single iron atom in the initial x-ray crystallographic model[7] and subsequently identified as a 2Fe-2S cluster by cryo-EM, although it still lacks any spectroscopic or kinetic signature. The periplasmic NqrC has one covalently bound FMN (FMN^{NqrC}) in its hydrophilic region[13,14]. The NqrB subunit is an integral membrane protein with a covalently bound FMN (FMN^{NqrB}) and a unique riboflavin cofactor (RBF^{NqrB}) that is the final donor of electrons to the ubiquinone (UQ) substrate[15,16]. The hydrophilic NqrA subunit is attached to the membrane through a tight interaction with the protruding part of the N-terminal region of NqrB. This cytoplasmic interfacial area has a significant influence on the binding of UQ[17,18]. These structural studies, along with earlier spectroscopic[19–23], kinetic[10,24], and mutagenetic investigations[8,9,12–14,25], have established a consensus electron transfer pathway: NADH → FAD^{NqrF} → $2Fe\text{-}2S^{NqrF}$ → $2Fe\text{-}2S^{NqrD/E}$ → FMN^{NqrC} → FMN^{NqrB} → RBF^{NqrB} → UQ.

However, the distances between two of the donor-acceptor pairs in two of these electron transfer steps: $2Fe\text{-}2S^{NqrF}$ → $2Fe\text{-}2S^{NqrD/E}$, and $2Fe\text{-}2S^{NqrD/E}$ → FMN^{NqrC}, shown as red arrows in Fig. 1a are too large (26-33 Å, edge-to-edge) for physiologically relevant electron transfer[7,25]. This indicates that the subunits containing these cofactors must undergo significant conformational rearrangements to reduce these spatial gaps during catalytic turnover[7,19]. Nevertheless, there is as yet no structural evidence to support these proposed rearrangements. In the case of the $2Fe\text{-}2S^{NqrF}$ → $2Fe\text{-}2S^{NqrD/E}$ electron transfer step, our

previous cryo-EM study of wild-type Na^+-NQR suggested that the cytosolic domain of the NqrF subunit is highly flexible, but the inferred range of motion is still not large enough to account for the electron transfer [7]. In the case of 2Fe-2S$^{NqrD/E}$ → FMN^{NqrC}, an apparent discrepancy between X-ray and cryo-EM results may actually indicate a crucial conformational change. In the X-ray crystallographic structures of *V. cholerae* Na^+-NQR[5,6], the periplasmic domain of NqrC containing FMN^{NqrC} is positioned near the NqrD/E subunits, whereas the cryo-EM structure places this domain near NqrB. These results suggest that repositioning of the NqrC subunit during turnover could allow FMN^{NqrC} to shuttle electrons from 2Fe-2S$^{NqrD/E}$ to FMN^{NqrB}. However, there is no evidence to link this apparent rearrangement of NqrC to different intermediates in the catalytic mechanism.

Another enigma involves in the pathway(s) for Na^+ translocation in the enzyme. Based on the biochemical characterization of conserved acidic residues within the TMHs, Juarez *et al.* identified critical acidic residues necessary for Na^+ translocation (e.g. NqrB-D397, NqrD-D133, and NqrE-E95)[26]. Hau *et al.* observed two bound Na^+ ions on the periplasmic side of NqrB in their cryo-EM map and proposed a Na^+ channel within NqrB[6]. More recently, Kumar et al. reported a cryo-EM structure of the "Rhodobacter nitrogen fixing" protein (RNF) complex, an evolutionary ancestor of Na^+-NQR[27]. Combined with atomic molecular dynamics (MD) simulations, they showed that the reduction of a 2Fe-2S cluster coordinated by the symmetric RnfA/E subunits (homologues of NqrD/E), induces capture of Na^+ and subsequently triggers an *inward/outward* transition of the subunits. This model aligns with the alternating-access mechanism proposed by Bogachev and colleagues for Na^+-NQR[10]. Despite numerous attempts to elucidate the mechanism of the redox-mediated Na^+ translocation in Na^+-NQR, no consensus has been reached. To address this, Na^+-NQR structures of different reaction states (or different reaction conditions) are needed.

In this study, we have combined cryo-EM and atomic-level MD simulations to show how each subunit undergoes conformational rearrangements that facilitate electron transfer within the enzyme and how these rearrangements drive Na^+ translocation. Our synergistic approach demonstrates that the reduction of the 2Fe-2S$^{NqrD/E}$ triggers Na^+ translocation across the membrane by coordinating with structural rearrangements in the NqrD/E subunits, which subsequently influence positioning of NqrC and NqrF. This study provides the first structural insights into the mechanism of Na^+ translocation coupled to electron transfer in Na^+-NQR.

102 **Abbreviations:** CBB, Coomassie Brilliant Blue; Cryo-EM, cryogenic electron microscope; DDM, *n*-
103 dodecyl *β*-maltoside; EPR, electron paramagnetic resonance; FAD, flavin adenine dinucleotide; FMN,
104 flavin mononucleotide; IC_{50}, the molar concentration needed to reduce the control enzymatic activity by
105 50%; MD, molecular dynamics; NADH, nicotinamide adenine dinucleotide reduced form; NAD^+,
106 nicotinamide adenine dinucleotide oxidized form; Na^+-NQR, Na^+-pumping NADH-ubiquinone
107 oxidoreductase; NTA, nitrilotriacetic acid; PAGE, polyacrylamide gel electrophoresis; RBF, riboflavin
108 RNF, Rhodobacter nitrogen fixing" protein; RT, room temperature; TMH, transmembrane helix; SDS,
109 sodium dodecyl sulfate; UQ, ubiquinone; UQH_2, ubiquinol (reduced form of ubiquinone); WT, wild-
110 type

RESULTS

Strategy for the preparation of cryo-EM grids

As described in the *Introduction*, structural studies on Na^+-NQR to date suggest that redox driven Na^+-translocation likely requires structural rearrangements in three different parts of the enzyme: the cytoplasmic domain of NqrF, the membrane embedded helices of NqrD/E, and the periplasmic region of NqrC, in order to modulate the distances between key pairs of redox cofactors: 2Fe-2S^{NqrF} to 2Fe-2S$^{NqrD/E}$ and 2Fe-2S$^{NqrD/E}$ to FMN^{NqrC} [7]. To capture snapshots of Na^+-NQR from *V. cholerae* in other putative conformational states, cryo-EM grids were prepared under nine different conditions that alter the catalytic cycle of the enzyme (Table 1): wild-type enzyme reduced by NADH in the presence (1) or absence (2) of Na^+ (**WT$_{red}$**, **WT$_{red}$/-Na$^+$**, respectively), (3) wild-type reduced by NADH in the presence of the inhibitor korormicin A (**WT$_{red}$+KR**), (4) wild-type reduced by NADH in the presence of the inhibitor aurachin D-42 (**WT$_{red}$+AD-42**), (5) NqrB-G141A reduced by NADH in the presence of korormicin A (**NqrB-G141A$_{red}$+KR**), NqrC-T225Y *as isolated* (6) or reduced (7) by NADH (**NqrC-T225Y$_{ox}$**, **NqrC-T225Y$_{red}$**, respectively), and NqrB-T236Y *as isolated* (8) or reduced (9) by NADH (**NqrB-T236Y$_{ox}$**, **NqrB-T236Y$_{red}$**, respectively).

The NqrC-T225Y and NqrB-T236Y mutants lack FMN^{NqrC} and FMN^{NqrB}, respectively, disrupting electron flow within the enzyme[19]. Korormicin A binds to the enzyme and allosterically inhibits the final electron transfer step in which ubiquinone becomes reduced[7,28]. The NqrB-G141A mutant exhibits significant resistance to korormicin A, though the inhibitor still binds to the enzyme[28]. These three mutations all interfere with the redox cycle of the enzyme and may thus be expected to influence the distributions in its conformational states. After the 3D reconstruction of particle images of the nine samples, each dataset was processed using the following analytical tools in the cryosparc soft[29] toolbox to isolate intermediate states in molecular motion: 3D variability analysis (3DV)[30], and 3DFlex (3DF)[31] (Extended Data Fig. 1, Supplementary Fig. 1,2, and Supplementary Table 1).

Structure of Na$^+$-NQR reduced by NADH

We determined the structure of wild-type enzyme reduced by 5 mM NADH (**WT$_{red}$**) at a resolution of 3.01 Å (Extended Data Fig. 1a and Supplementary Fig. 1a). As all the spectroscopically visible cofactors in Na^+-NQR are reported to be fully reduced under these conditions[19], this structure is thought to represent the fully reduced structure of the enzyme. The overall structure is very close to that of the enzyme *as isolated* (**WT$_{ox}$,** PDB ID: 7XK3), with a single, well-resolved state observed for the NqrC subunit (Extended Data Fig. 2a). In the structure of **WT$_{red}$**, NADH is bound in a long flat density around the Rossmann nucleotide binding motif of NqrF[8] (Supplementary Fig. 3). Focusing on the membrane domain, the TMH bundle formed by NqrF, NqrD/E, and NqrC (TMH^{NqrCDEF} bundle) has a structure consistent with an *"inward-open"* state. Notably, TMHs 3-4 of NqrE on the cytoplasmic side have

shifted slightly toward 2Fe-2S$^{NqrD/E}$ compared to the **WT$_{ox}$** structure (Extended Data Fig. 2a).

NqrF is a cytoplasmic subunit anchored to the membrane by a single transmembrane helix (TMH1^{NqrF}). It is also tightly bound to the neighboring hydrophilic NqrA subunit through electrostatic interactions. The hydrophilic part of NqrF is highly flexible and comprises two distinct domains: a ferredoxin-NADPH reductase (FNR)-like domain (K132−G408) containing the FAD cofactor, and a ferredoxin-like domain (G33−K131) harboring the 2Fe-2S^{NqrF} as its cofactor[8,9] (Fig. 1b).

In the currently obtained cryo-EM structures, including that of fully reduced state (**WT$_{red}$**), the NqrF subunit displays high conformational flexibility, adopting multiple distinct states. Nevertheless, the extent of flexibility does not extend into the membrane region as would be necessary for electron transfer. The distance between 2Fe-2S^{NqrF} and the 2Fe-2S$^{NqrD/E}$, even at their closest proximity, is 30 Å (edge to edge), which is inconsistent with catalytic turnover rates. Therefore, during the catalytic cycle, NqrF likely undergoes a pivotal motion of its ferredoxin-like domain between FAD and 2Fe-2S$^{NqrD/E}$, while the TMH1^{NqrF} remains firmly anchored to the membrane. However, the electron transfer in NqrF is too fast (below milliseconds) to capture the snapshot in motion[21].

Resolution of three conformations of the cytoplasmic NqrF subunit

To capture such rapid motions of NqrF, Na^+-NQR was reduced by 5 mM NADH in the absence of Na^+ (**WT$_{red}$/-Na$^+$**). In these conditions, the rate constant for FMN^{NqrC} reduction is slowed approximately eightfold[19], which may allow the identification of previously unobserved conformational states of NqrF. By focusing on the position of the ferredoxin-like domain, three distinct states of NqrF—***up***, ***middle***, and ***down***—were identified as separate classes (Fig. 1b,c, Extended Data Fig. 1b, and Supplementary Fig. 1b). These continuous density maps were further refined using 3DF (Supplementary Fig. 2a).

The *"**up**"* state comprises over 87% of the particle population in the dataset, providing a high-resolution map at 2.65 Å, where the FNR-like and ferredoxin-like domains are found in similar positions to those in the enzyme *as isolated* (**WT$_{ox}$**). The *"**down**"* state, reconstructed from the smallest population of the particles (5%), gave a final density map at 3.11 Å. Remarkably, in the "***down***" state, the ferredoxin-like domain fits into the pocket formed by the NqrD/E subunits, whereas this pocket is exposed to the cytoplasm in the other two states. Consequently, the distance between 2Fe-2S^{NqrF} and 2Fe-2S$^{NqrD/E}$ is reduced to 16.6 Å, consistent with electron transfer between them, while the distance between FAD^{NqrF} and 2Fe-2S^{NqrF} is increased to 31.0 Å (Fig. 1c). Although the resolution of the *"**middle**"* state is relatively low (3.75 Å), the density map is sufficient to position the ferredoxin-like domain in an intermediate location between the *"**down**"* and *"**up**"* states (Fig. 1b,c).

Notably, in all three states, the structures of the membrane domains, including TMH^{NqrF}, remain almost identical to those in **WT$_{red}$**, with the TMH^{NqrCDEF} bundle in an *"inward-open"* state (Fig. 2 and Extended Data Fig. 2b,c). This shows that the reduction of the NqrF cofactors allows the ferredoxin-like

domain harboring 2Fe-2S^{NqrF} to bridge transport of electrons from FAD^{NqrF} to 2Fe-2S$^{NqrD/E}$, without altering the conformation of the TMH^{NqrCDEF} bundle.

The conformational shift of the NqrC subunit between NqrB and NqrD/E

Korormicin A (KR) and aurachin D-42 (AD-42) are specific inhibitors of Na^+-NQR that can serve as tools for capturing key reaction intermediates of the enzyme[32–37]. However, wild-type enzyme with korormicin A or aurachin D-42 bound (**WT$_{red}$ + KR**, **WT$_{red}$ + AD-42**), treated with NADH, did not show any distinct reaction intermediates (Extended Data Fig 1c,d and 2h,i and Supplementary Fig 1c,d, and 4), as the inhibitor completely terminates UQ reduction at the final step of the catalytic cycle, mimicking **WT$_{red}$**. To decelerate the catalytic cycle of Na^+-NQR, we prepared a cryo-EM grid of the NADH-treated NqrB-G141A mutant with korormicin A bound (**NqrB-G141A$_{red}$ + KR**). This alanine substitution excludes the alkyl side chain of korormicin A from the binding cavity (Supplementary Fig 5), resulting in a decrease in the binding affinity (~160-fold increase in IC_{50} values) although the inhibitor molecule still binds to the mutated enzyme[28,38–40]. This unique combination of mutation and inhibitor could potentially influence the catalytic cycle of the enzyme, and lead to the identification of multiple conformational states of the enzyme.

The image particles were processed through iterative 3DV with a mask covering the entire Na^+-NQR complex, followed by focused refinement on the NqrC density. This approach identified two distinct states of Na^+-NQR, one in which the hydrophilic domain of the NqrC subunit approaches the NqrD/E and one in which it approaches NqrB, likely reflecting its motion during catalytic turnover (Extended Data Fig. 1e, Supplementary Fig. 1e, Supplementary Video 1). These continuous density maps were further refined by 3DF (Supplementary Fig. 2b) to reconstitute two conformational states: *"**stable**"* and "***shifted***" with particle populations of 88 and 12%, respectively (Fig. 3).

In the "***stable***" state (Fig. 3b), resolved at 2.93 Å, the NqrC subunit has moved closer to NqrB, consistent with rapid electron transfer between FMN^{NqrC} and FMN^{NqrB} (7.8 Å). This structure aligns with that of the enzyme treated with NADH (**WT$_{red}$**). In contrast, the "***shifted***" state, reconstructed at 2.61 Å with improved local alignment of particle images, exhibits a weaker density for the hydrophilic domain of NqrC, suggesting increased flexibility in this region. This flexibility makes full *de novo* modeling challenging; however, a structural model with rigid body fitting indicates that the hydrophilic domain of NqrC subunit has shifted toward the NqrD/E subunits.

In the ***shifted*** state (Fig. 3b), while FMN^{NqrC} remains distant from 2Fe-2S$^{NqrD/E}$ (~27 Å), the loop of Glu169-Gly177^{NqrC}, which includes Thr173 and Leu176 that stabilize the isoalloxazine ring of this FMN[9], is embedded in the pocket formed by the NqrD/E subunits. The existence of these two distinct conformations shows that the periplasmic domain of NqrC, which houses FMN^{NqrC}, switches its position between NqrB and NqrD/E in a way that allows it to mediate electron transfer from 2Fe-2S$^{NqrD/E}$ to

216 FMN^{NqrB} (Fig. 1a, 3). Notably, the $TMH^{NqrCDEF}$ bundle adopts the *"inward-open"* conformation in the
217 "***stable***" state but transitions to the *"outward-open"* conformation in the "***shifted***" state (Fig. 2). This
218 *inward-to-outward* transition of the bundle appears to be linked to the relocation of the periplasmic
219 domain of NqrC from the NqrB side to the NqrD/E side.
220
221 ***The rearrangement of NqrC is coordinated with the inward/outward transition of the $TMH^{NqrCDEF}$***
222 ***bundle***
223 To understand the factors that could cause NqrC to move from the NqrB side to the NqrD/E side, we
224 analyzed the structure of mutants lacking either FMN^{NqrB} (NqrB-T236Y) or FMN^{NqrC} (NqrC-T225Y). In
225 the mutant lacking FMN^{NqrB} (Extended Data Fig 3a)[34–36], both "*as isolated*" and "NADH-treated"
226 enzymes (**NqrB-T236Y_{ox}** and **NqrB-T236Y_{red}**) showed *"inward open"* structures with the NqrC
227 subunits positioned near NqrB at resolutions of 3.83- and 3.31-Å, respectively (Extended Data Fig. 1f,g
228 and 2d,e and Supplementary Fig 1f,g). These structures closely resemble **WT_{ox}** and **WT_{red}**
229 (Supplementary Fig. 6), suggesting that this mutant adopts a similar conformation in which NqrC has
230 shifted fully from the NqrD/E side to the NqrB side. In contrast, the mutant lacking FMN^{NqrC} (Extended
231 Data Fig. 3b) show identical *outward-open* structures with NqrC shifted toward NqrD/E, irrespective of
232 NADH treatment (**NqrC-T225Y_{ox}** and **NqrC-T225Y_{red}**) with resolutions of 2.66- and 2.59-Å,
233 respectively (Extended Data Fig 1h,i and 2f,g, Supplementary Fig. 1h,i). In these conformations, as in
234 the "***shifted***" state in **NqrB-G141A_{red} + KR**, the periplasmic domain of NqrC is positioned closest to
235 the dimetric NqrD/E subunits (Fig. 3b and Extended Data Fig 3c).
236 These findings, including the structure of the korormicin A-bound NqrB-G141A mutant (**NqrB-**
237 **G141A_{red} + KR**), suggest that the rearrangement of NqrC is coupled to the *inward-to-outward* transition
238 of the NqrD/E subunits, which bind $2Fe\text{-}2S^{NqrD/E}$. In the structure of Na^+-NQR reduced by NADH in the
239 absence of Na^+ (**WT_{red}/-Na^+**), all observed NqrF states (***up, middle,*** and ***down***) corresponded to the
240 *inward-open* state of the $TMH^{NqrCDEF}$ bundle (Fig. 2, Extended Data Fig. 2a-c), suggesting that the
241 position of $2Fe\text{-}2S^{NqrF}$ does not influence the membrane domain structure. Considering that electron
242 transfer from $2Fe\text{-}2S^{NqrD/E}$ to FMN^{NqrC} requires conformational rearrangements of both NqrC and
243 NqrD/E, it is plausible that, the redox state of $2Fe\text{-}2S^{NqrD/E}$ may drive the *inward-to-outward* transition
244 of the $TMH^{NqrCDEF}$ bundle. This transition likely triggers the relocation of the periplasmic domain of
245 NqrC, thereby facilitating the reduction of FMN^{NqrC}.
246
247 ***Shift in local resolution map reflects redox driven conformational changes of Na^+-NQR***
248 During single-particle analysis, we noticed that some of the redox-induced rearrangements of Na^+-
249 NQR subunits correlate with shifts in the local resolution map. A notable example of this is the
250 rearrangement of NqrF during electron transfer from FAD to $2Fe\text{-}2S^{NqrD/E}$ (Fig. 1b,c). In the "***down***" and

"***middle***" states, where 2Fe-2S^{NqrF} is positioned close enough to 2Fe-2S$^{NqrD/E}$ to allow facile electron transfer, the ferredoxin-like domain of NqrF shows lower resolution, while the FNR-like domain containing FAD remains highly resolved (Supplementary Fig. 2a). This suggests that reduction of 2Fe-2S^{NqrF} increases the flexibility of the ferredoxin-like domain, enabling its movement towards 2Fe-2S$^{NqrD/E}$, while the FNR-like domain remains stable, preventing electron backflow.

Interestingly, this observation is even more pronounced in the structure of the NqrB-G141A mutant with bound korormicin A (**NqrB-G141A$_{red}$ + KR**), which exhibits two distinct states of the TMH^{NqrCDEF} bundle. In the "***stable***" state, where the bundle adopts an "*inward-open*" conformation, the cytoplasmic domain of NqrF appears blurred (flexible), whereas the periplasmic domain of NqrC exhibits sharp density (rigid). Conversely, in the "***shifted***" state, where the bundle adopts an "*outward-open*" conformation, NqrF displays sharp density (rigid), while NqrC appears blurred (flexible) (Extended Data Fig. 1e, Supplementary Fig 1e, and 2b).

A similar pattern appears in the NqrC-T225Y mutant, which lacks FMN^{NqrC}. This mutant adopts the "*outward-open*" conformation of its TMH^{NqrCDEF} bundle, similar to the "***shifted***" state, and shows the highest resolution for NqrF, indicating that it remains in a single, stable "***up***" conformation (Extended Data Fig 1h,i, Supplementary Fig 1h,i). Together, these results suggest that the "*inward-to-outward*" transition alternates the flexibility of NqrF and NqrC, coordinating electron transfer from 2Fe-2S^{NqrF} to FMN^{NqrC} via 2Fe-2S$^{NqrD/E}$. The shifting resolution patterns highlight how structural flexibility and stability work together to control electron flow.

A proposed mechanism for Na$^+$ translocation

Recently, Müller and coworkers published a cryo-EM structure of the RNF complex from *A. woodii*, where the RnfA/E subunits coordinating a 2Fe-2S cluster show high homology to the NqrD/E subunits of Na$^+$-NQR[27]. Long-range molecular dynamics (MD) simulations predicted that the dimeric RnfA/E subunits can adopt two distinct conformations—*inward-* and *outward-open*—depending on the redox state of the 2Fe-2S cluster. This rearrangement appears to be crucial for both Na$^+$ translocation and electron transfer within the enzyme. Their report supports the hypothesis that, in Na$^+$-NQR, the redox state of the 2Fe-2S$^{NqrD/E}$ not only drives the *inward-to-outward* transition of TMHs^{NqrCDEF} bundle but also facilitates Na$^+$ translocation.

We have performed MD simulations beginning from the cryo-EM structure with an *inward-open* state of TMHs^{NqrCDEF} bundle, which provide some insight into the mechanism of Na$^+$ uptake from the cytoplasm (Supplementary Table 2). Spatial density analysis of MD simulations results showed that Na$^+$ ions and water can access the cytoplasmic pocket near 2Fe-2S$^{NqrD/E}$ in the wild-type Na$^+$-NQR with reduced 2Fe-2S^{NqrF} and 2Fe-2S$^{NqrD/E}$ (Fig. 4a,b). The reduction of 2Fe-2S$^{NqrD/E}$ is linked to formation of a Na$^+$ binding site on the cytoplasmic side. In contrast, Na$^+$ ions could not fully access the cytoplasmic

286 pocket with the oxidized 2Fe-2S$^{NqrD/E}$ (Supplementary Fig 7). Pairs of hydrophobic residues, that could
287 function as gates for cation movement, are found above and below the Na^+ binding site: Leu26^{NqrD}-
288 Leu115^{NqrE} and Leu107^{NqrD}-Leu23^{NqrE} (Fig. 4f). These residues control the access of Na^+ ions and water
289 and are conserved between NQR and RNF (Supplementary Fig 8).

290 Because the spontaneous *inward-to-outward* transition of the TMH^{NqrCDEF} bundle was not observed
291 within the time scale of simulations, we employed targeted MD (TMD) simulation to induce this
292 conformational transition[41]. During the TMD simulation, an external force was applied to make the
293 conformation of NqrD/E move toward the *outward-open* state. During the TMD and subsequent
294 equilibrium simulations, the inside gate closed while the outside gate opened (Fig. 4c,f,g, and Extended
295 Data Fig. 4). The conformational transition shifted the bound Na^+ to the outward side of the binding site
296 relative to 2Fe-2S$^{NqrD/E}$ (Fig. 4d,g). With the oxidation of 2Fe-2S$^{NqrD/E}$, the bound Na^+ was eventually
297 released to the outer side of the membrane (Fig. 4h). Na^+ translocation was observed in two additional
298 independent trajectories following the TMD simulation (Supplementary Fig. 9). It is noteworthy that the
299 Na^+ ion was partially hydrated during the translocation with two or more coordinated water molecules
300 (Fig. 4e). This may be due to the lack of acidic residues in the binding site that would strongly bind the
301 ion and dehydrate it as in some transporter proteins[42]. Instead, the binding site is made up of backbone
302 atoms of Thr110^{NqrD}, Cys112^{NqrD}, Val118^{NqrE}, and Cys120^{NqrE} (Fig. 4f–h and Extended Data Fig 5).

DISCUSSION

The overall reaction mechanism of Na^+-NQR

Since the first publication of a structural model of Na^+-NQR, it has been clear from the spatial arrangement of the redox cofactors that structural rearrangements would have to play a critical role in the enzyme and that understanding these conformational changes would be essential to elucidating the mechanism of redox-driven Na^+ pumping. In this study, we have identified at least five distinct conformational states of Na^+-NQR, which may reflect key reaction steps of the enzyme. Based on the multiple conformations of Na^+-NQR revealed by the current cryo-EM work and previous studies[9], together with MD simulations, we propose an overall reaction mechanism for the enzyme, which progresses through six key steps (Fig. 5 and Supplementary Fig. 10).

Step 1 (Oxidized state): In the absence of NADH, all cofactors—except for RBF, which is present as a stable neutral semiquinone[15]—are fully oxidized. In this form, the dimeric NqrD/E subunits are in an *inward-open* state. The hydrophilic domain of NqrF remains flexible and does not adopt a distinct structure; however, the range of motion of NqrF does not bring it into proximity with the NqrD/E subunits.

Step 2 (NADH binding): When NADH binds to the NqrF subunit, it donates two electrons. One electron is transferred to the $2Fe\text{-}2S^{NqrF}$, increasing the flexibility of the ferredoxin-like domain of NqrF, allowing it to approach NqrD/E.

Step 3 (Na^+ uptake): The highly flexible ferredoxin-like domain of NqrF approaches the cytoplasmic pocket formed by the dimeric NqrD/E. This rearrangement allows electron transfer from $2Fe\text{-}2S^{NqrF}$ to $2Fe\text{-}2S^{NqrD/E}$. The negative charge on the reduced $2Fe\text{-}2S^{NqrD/E}$ enables accommodation of hydrated Na^+ between inward and outward gates, which are made up of conserved hydrophobic amino acids.

Step 4 (Transition to outward-open conformation and Na^+ release): The NqrD/E subunits, upon reduction of $2Fe\text{-}2S^{NqrD/E}$ and binding of Na^+, undergo a conformational switch to the *outward-open* state, exposing the bound Na^+ to the periplasmic side. This transition increases the flexibility of hydrophilic domain of NqrC, enabling its approach toward NqrD/E, while the flexibility of NqrF decreases, preventing electron backflow into $2Fe\text{-}2S^{NqrF}$. This Na^+- and redox-dependent repositioning of NqrC allows electron transfer from $2Fe\text{-}2S^{NqrD/E}$ to FMN^{NqrC}. Simultaneously, the bound Na^+ loses affinity and is released to the periplasm following reoxidation of $2Fe\text{-}2S^{NqrD/E}$.

Step 5 (return to inward-open conformation):

This reoxidation also induces a conformational relaxation of the NqrD/E subunits, restoring them to the *inward-open* state and allowing NqrC to return to the NqrB side. This movement facilitates electron transfer from FMN^{NqrC} to RBF^{NqrB} via FMN^{NqrB}. Since i) the UQ reduction is a two-electron process while ii) FMNs and RBF undergo single-electron redox reaction[20], a similar series of

338 reactions (from Steps 2 to 5) repeats to the transfer of a second electron, which is coupled with the
339 translocation of second Na^+.
340 ***Step 6 (UQ reduction):*** Through two sequential redox cycles from 2Fe-2S^{NqrF} to RBF^{NqrB}, UQ
341 accepts two electrons to form UQH_2, which is then released from the enzyme. Thus, the enzyme
342 returns to the initial oxidized state. Although the structure of Na^+-NQR with bound UQ has not yet
343 been identified, photoaffinity labeling experiments suggest that the UQ head-ring is positioned
344 within a pocket in the NqrA subunit, approximately 20 Å above the membrane surface. Note that
345 Hau et al. reported a structure of UQ_2-bound Na^+-NQR, in which UQ_2 was modeled inside the
346 inhibitor binding pocket in the *N*-terminal region of NqrB[6]. However, the density map of UQ_2
347 molecule in the pocket is too weak to definitely model UQ_2 molecule. It is, therefore, premature to
348 conclude that UQs accept electrons from RBF in the inhibitor binding pocket in NqrB.
349
350 ***Na^+-translocating pathway***
351 The mechanism of redox-driven Na^+ translocation by Na^+-NQR remains to be fully elucidated. Based
352 on the X-ray crystallographic and cryo-EM models, Fritz and colleagues proposed that cytoplasmic Na^+
353 is translocated to the periplasm via a pathway within NqrB, where it is coordinated by residues such as
354 Ile371, Arg372, Pro376, and Tyr378[5,6]. Our MD simulations also identified Na^+ binding to periplasmic
355 residues of NqrB, such as Thr236 and Ser239 (Fig. 4a,b, Extended Data Fig 5, Supplementary Fig. 7
356 and 11 and Supplementary Table 3). However, this Na^+ was consistently observed across all enzyme
357 states identified in this study, indicating that NqrB is unlikely to be directly involved in redox-driven
358 Na^+ translocation across the membrane. We were unable to identify any continuous ion translocation
359 pathway spanning the transmembrane region of NqrB, but we have found a pathway of this kind at the
360 interface between the NqrD/E subunits. Consistent with the recent study on the *A. woodii* RNF
361 complex[27], our findings strongly suggest that Na^+ translocation is mediated exclusively by the NqrD/E
362 subunits, rather than by NqrB.
363 The redox-dependent *inward-to-outward* transition of the TMH^{NqrCDEF} bundle was not observed in our
364 MD simulations. During structural modeling of Na^+-NQR in the inward- and outward-open states, we
365 noticed that the conformation of the NqrD/E subunits appeares to undergo a conformational change
366 centered on Prolines in TMH4 of NqrE—a highly conserved residue located near the 2Fe-2S$^{NqrD/E}$ and
367 surrounded by hydrophobic residues (Fig. 5b, and Supplementary Fig. 8). A change in the redox state of
368 2Fe-2S$^{NqrD/E}$ may be linked to subtle local rearrangement in adjacent amino acid residues by through
369 electrostatic interactions, and these rearrangements could be amplified by conserved proline, leading to
370 larger conformational shifts. A similar proline-mediated switching mechanism has been proposed in the
371 structure of voltage-gated potassium (Kv) chanel[43].
372 Finally, we address how Na^+ is translocated against the sodium motive force (Na^+ gradient across the

membrane). Our findings indicate that the "*inward-to-outward*" transition of the $TMH^{NqrCDEF}$ bundle alternately regulates the flexibility of the NqrF and NqrC subunits to control electron flow. This mechanism likely essential for the redox-driven Na^+ translocation—namely, that electron does not flow forward without Na^+ being expelled to the periplasm. For instance, in the *outward-open* conformation with periplasmic Na^+ bound, electron backflow from $2Fe\text{-}2S^{NqrD/E}$ to $2Fe\text{-}2S^{NqrF}$ would be necessary to trigger the transition to the *inward-open* conformation, that would allow the bound Na^+ to move back toward the cytoplasm. Nevertheless, as NqrF is firmly stabilized in this state, such electron backflow may not take place.

In summary, the present structural analyses of Na^+-NQR in multiple distinct conformations, combined with MD simulations, provide critical insights into the coupling mechanism between the electron transfer and Na^+ translocation. These findings illustrate how structural rearrangements of individual subunits can control Na^+ translocation and electron transfer, to achieve coupling between the two processes. This study establishes a valuable framework for further mechanistic studies of Na^+-NQR and antibiotics development targeting the enzyme.

388 **METHODS**

389 ***Na^+-NQR expression and purification***

390 Expression of *Vibrio cholerae* Na^+-NQR from a plasmid, in the parent organism, construction of site-
391 specific mutants, and cultivation of *V. cholerae* strains have been described previously (REF)[7]. Na^+-
392 NQR was purified as previously described. The membrane pellets were solubilized in a buffer containing
393 50mM NaPi, 300mM NaCl, 5.0mM imidazole, and protease inhibitor cocktail (Sigma-Aldrich), 0.4%
394 (w/v) *n*-dodecyl- β-D-maltoside (DDM), pH 8.0, with stirring for 1 h at 4 ˚C. The mixture was clarified
395 by ultracentrifugation (100,000 g), and the supernatant was mixed with 20 mL of Ni-NTA resin (Qiagen)
396 that had been equilibrated with binding buffer (50mM NaPi, 300mM NaCl, 5.0mM imidazole, and
397 0.05% DDM). After gentle agitation for 1 h at 4 ˚C, the suspension was poured into an empty plastic
398 column. The column was washed with 4 volumes of the binding buffer, followed by 5 volumes of a
399 wash buffer (same as binding buffer but containing 10mM imidazole). The protein was eluted from the
400 column using an elution buffer (same as binding buffer but containing 100 mM imidazole). The resulting
401 Na^+-NQR preparation was applied to a DEAE anion exchange column (HiPrep DEAE FF 16/10,
402 connected to an ÄKTA system, Cytiva) equilibrated with buffer A [50 mM Tris/HCl, 1.0 mM EDTA,
403 5% (v/v) glycerol, and 0.05% (w/v) DDM, pH 8.0]. The protein was eluted with a linear gradient of
404 buffer B (buffer A containing 2.0 M NaCl), and the fractions containing pure Na^+-NQR were pooled and
405 concentrated to 15~20 mg of protein/mL. Subunit assembly was confirmed by SDS-PAGE[44] and enzyme
406 activity was checked by the inhibitors-sensitive NADH-UQ_1 oxidoreductase activity measurements at
407 282 nm ($\varepsilon = 14.5 mM^{-1}cm^{-1}$)[2]. To remove glycerol from samples, the target protein was further separated
408 by size-exclusion chromatography (Superose™ 6 increase 10/300 gel filtration column, Cytiva) with an
409 elution buffer containing 50 mM Tris-HCl, 100 mM NaCl, 1.0 mM EDTA, 0.05% DDM (pH 8.0).
410

411 ***Cryo-EM acquisition***

412 To reduced DDM concentrations, immediately prior to cryo-EM grid preparation, all of the purified Na^+-
413 NQR samples were washed with the same elution buffer without detergent (50 mM Tris-HCl, 100 mM
414 NaCl, 1.0 mM EDTA, pH 8.0). To obtain the reduced form of Na^+-NQR, Na^+-NQR solution was mixed
415 with an NADH solution to final concentration of 5 mM just before application onto a grid. 2.7 μL of
416 Na^+-NQR solution at the concentration of 10 mg/mL was applied onto a glow-charged Quantifoil Cu
417 R1.2/1.3. The grid was blotted by Vitrobot IV and vitrified with liquid ethane. Cryo-EM movies were
418 acquired with a Titan Krios electron microscope (Thermo Fisher, USA) equipped with K3 BioQuantum
419 camera (Gatan, United States). Data collection was automatically controlled by SerialEM software at a
420 nominal magnification of 81,000 and the pixel size is 0.88 Å/pix. The total electron dose and frame rate
421 were 60 electron/$Å^2$ and 0.1 s, respectively.
422

Cryo-EM data processing

The details of image processing steps in each condition are shown in Extended Data Fig. 1. All of seven datasets （**WT_{red}, WT_{red}/ -Na^+, WT_{red} + KR, WT_{red} + AD-42, NqrB-G141A_{red} + KR, NqrB-T236Y_{ox}, NqrB-T236Y_{red}, NqrC-T225Y_{ox}**, and **NqrC-T225Y_{red}**） were processed by cryoSPARC v3.3.1 or v4.0. 6,086, 13,302, 4,881, 5,096, 13,316, 4,440, 8,212, 13,302, and 5,086 movies were used for data analyses, respectively. After motion correction, CTF estimation, and manually curate exposures, the machine-learning-based particle picking by Topaz software extracted 1,391,844, 2,497,690, 2,157,492, 1,072,343, 2,378,419, 1,026,158, 2,496,421, 3,653,368, and 1,384,33 particles from the datasets, respectively. After particle selections with Heterogeneous Refinement and Ab-initio Reconstruction at the class similarity of 0.6, selected better particles were used in Non-uniform Refinement with the optimizing per-particle defocus option. The datasets having weak density regions were classified with 3DV or 3DC, and the components having stronger density were refined by Local refinement, and/or Non-uniform Refinement. Finally, all datasets provided density maps at 3.07- (**WT_{red},**), 2.65- (***up* state of WT_{red}/ -Na^+**), 3.75- (***middle* state of WT_{red}/ -Na^+**), 3.11- (***down* state of WT_{red}/ -Na^+**), 2.90- (**WT_{red} + KR**), 2.74- (**WT_{red} + AD-42**), 2.61- (***stable* state of NqrB-G141A_{red} + KR**), 2.93- (***shifted* state of NqrB-G141A_{red} + KR**), 3.83- (**NqrB-T236Y_{ox}**), 3.31- (**NqrB-T236Y_{red}**), 2.66- (**NqrC-T225Y_{ox}**), and 2.59- (**NqrC-T225Y_{red}**) Å resolution, respectively. These resolutions were estimated based on the gold standard criteria (FSC = 0.143). Furthermore, to capture the overall structure of flexible NqrF subunits, non-uniform refined models (**WT_{red}/ -Na^+**, and **NqrB-G141A_{red} + KR**) were reconstructed with 3DFlex Refinement using a mask covering all subunits. The Flex maps provided by 3DFlex reconstruction are referenced for model building.

Model building and refinement

The atomic models were built based on our previous cryo-EM structures of Na^+-NQR (PDB ID: 7XK3 - 7). The initial models were fitted into the density maps with the Chain Refine and Space Refine Zone functions of COOT software[45]. The parts containing weak densities were adjusted with rigid body fitting and morphing. The Flex map output from 3DFlex Reconstruction was used to model the heterogeneous conformations with flexibility. Using the phenix_real_space_refine program[46], the corrected models were refined with secondary structure and Ramachandran restraints. These results were manually validated with COOT. The iteration of model refinement provided the correct models following the geometry. The model validation was evaluated with Molplobity[47]. To avoid over-fitting, the final models were validated with Fourier shell correlation computed from the final density maps. The model statistics are shown in Supplementary Table 1. Images of structures were generated with UCSF chimeraX software[48]. UCSF ChimeraX was used to compute the electrostatic potential, with default parameters and the Coulombic command with a range of −10 to 10 kcal/(mol·e).

458 ***Molecular dynamics simulation***

459 The all-atom MD simulations of the Na^+-NQR complex were performed using the cryo-EM structure
460 (PDB ID: 7XK3) and the crystal structure (PDB ID: 8ACW) as the initial structures. For modeling of
461 missing residues at the N-termini (for NqrB, NqrC, and NqrD) and C-termini (for NqrB and NqrC),
462 GalxyFill plug in CHARMM-GUI[49] was used. The cofactors (FAD, $2Fe–2S^{NqrF}$, $2Fe–2S^{NqrD/E}$, FMN^{NqrC},
463 FMN^{NqrB}, and RBF) were retained as in the PDB structures. The Nqr structure was embedded in a 150
464 × 150 Å POPC membrane and solvated with TIP3P water and 150 mM sodium and chloride ions with
465 the Membrane Builder plugin in CHARMM-GUI[50,51]. The CHARMM36 force field[52] was used except
466 for the cofactors whose parameters were adapted from the works of Kaila group[27,53,54]. The total number
467 of atoms is ~380,000.

468 The systems were energy minimized with the restraint of non–hydrogen POPC, protein, and cofactor
469 atoms for 10,000 steps. Then, they were equilibrated in three stages: (1) 100 ps equilibration at T = 150
470 K and no pressure control with the restraint of non–hydrogen POPC, protein, and cofactor atoms, (2)
471 500 ps equilibration at T = 310 K and 1 bar pressure with the restraint of non–hydrogen protein and
472 cofactor atoms, (3) 500 ps equilibration at T = 310 K and 1 bar pressure with the restraint of protein–Cα
473 and non–hydrogen cofactor atoms. The restraint force constant was 1.0 kcal mol^{-1} $Å^{-2}$ for each atom. The
474 production runs were performed at T = 310 K and 1 bar pressure without restraints. Long-range
475 electrostatic interactions were calculated by the particle mesh Ewald method[55] with a direct space cut
476 off of 12 Å. Langevin dynamics with 1 ps^{-1} damping coefficient was used for temperature control at T
477 = 310 K, and the Nosé–Hoover Langevin piston was used for pressure control at 1 bar[56—58]. The
478 integration timestep was set to 2 fs by applying the SHAKE method[59] to bonds involving hydrogen.
479 Targeted MD (TMD) simulations were also performed using an outward-open conformation of NqrD/E
480 (shifted state of NqrB-G141A_{red} + KR) as the reference. The force constant for TMD force was set to
481 500 kcal mol^{-1} $Å^{-2}$ and applied to the Cα atoms of NqrD and NqrE. All MD simulations were performed
482 using NAMD 2.12 /2.14/ 3.0[60].

483

Data availability: The cryo-EM maps have been deposited in the EMDB under accession codes, 64518 (**WT$_{red}$**), 63872 (**NqrC-T225Y$_{ox}$**), 64059 (**NqrC-T225Y$_{red}$**), 64060 (**NqrB-T236Y$_{ox}$**), 64061 (**NqrB-T236Y$_{red}$**), 64063 (**WT$_{red}$/ -Na^{+}**, "*up*" state), 64064 (**WT$_{red}$/ -Na^{+}**, "*middle*" state), 64065 (**WT$_{red}$/ -Na^{+}**, "*down*" state), 64062 (**WT$_{red}$ + KR**), 64069 (**WT$_{red}$ + AD-42**), 64066 (**NqrB-G141A$_{red}$ + KR**, "*stable*" state), and 64068 (**NqrB-G141A$_{red}$ + KR**, "*shifted*" state). The atomic models have been deposited in the Protein Data Bank under accession codes, 9UUU (**WT$_{red}$**), 9U5G (**NqrC-T225Y$_{ox}$**), 9UD2 (**NqrC-T225Y$_{red}$**), 9UD3 (**NqrB-T236Y$_{ox}$**), 9UD4 (**NqrB-T236Y$_{red}$**), 9UD6 (**WT$_{red}$/ -Na^{+}**, "*up*" state), 9UD8 (**WT$_{red}$/ -Na^{+}**, "*middle*" state), 9UD9 (**WT$_{red}$/ -Na^{+}**, "*down*" state), 9UD5 (**WT$_{red}$ + KR**), 9UDG (**WT$_{red}$ + AD-42**), 9UDA (**NqrB-G141A$_{red}$ + KR**, "*stable*" state), and 9UDF (**NqrB-G141A$_{red}$ + KR**, "*shifted*" state). The initial model of Na^{+}-NQR with and without bound inhibitors for model building is accessible in PDB under accession number 7XK3 (oxidized form of Na^{+}-NQR: **WT$_{ox}$**[7]), 7XK6 (oxidized form of Na^{+}-NQR with bound AD-42: **WT$_{ox}$ + AD-42**), and 7XK7 (oxidized form of Na^{+}-NQR with bound KR: **WT$_{ox}$ + KR**) [9]. The data that support the findings of this study are available from the corresponding author upon reasonable request.

Acknowledgements: We thank Dr. Joel E. Morgan (Rensselaer Polytechnique Institute) for the valuable discussion and comments during this work. We acknowledge the Research Support Project for Life Science and Drug Discovery (Basis for Supporting Innovative Drug Discovery and Life Science Research (BINDS)) from AMED under Grant Number JP23ama 121001. The computation was performed at the Research Center for Computational Science, Okazaki, Japan (Project: 24-IMS-C198, 25-IMS-C227). This work was financially supported by JSPS KAKENHI (22KJ1795 to M.I-F, 24K08729 to T.M., 23K23858 and 25H02299 to K.O., 21H02130 to H.M., and 25K01958 to M.M.), the Uehara Memorial Foundation (to J.K.), Takeda Science Foundation (to J.K.), and the National Institutes of Health (R56-AI132580 and R01AI181279 to B.B.).

Author contributions: M.I-F., J.K., T.M., B.B. H.M., and M.M. designed the research; M.I-F., T.M., and B.B expressed and purified Na^{+}-NQR; M.I-F., J.K., and T.M. performed structural determination and built the atomic models; T.S. and O.K. performed MD simulation; M.I-F., T.S., J.K, T.M., K.O, T. K., B.B., H.M. and M.M analyzed data; K.J. and M.M. directed the project and wrote the paper with M I-F., T.M., K.O., B.B. and H.M.

515 **REFERENCES**

1. Hayashi, M., Nakayama, Y., and Unemoto, T. Recent progress in the Na^+-translocating NADH-quinone reductase from the marine *Vibrio alginolyticus*. *Biochim. Biophys. Acta (Bioenerg.)* **1505**, 37–44 (2001).
2. Juárez, O., and Barquera, B. Insights into the mechanism of electron transfer and sodium translocation of the Na^+-pumping NADH-quinone oxidoreductase. *Biochim. Biophys. Acta (Bioenerg.)* **1817**, 1823–1832 (2012).
3. Dibrov, P., Dibrov, E., and Pierce, G. N. Na^+-NQR (Na^+-translocating NADH:uniquinone oxidoreductase) as a novel target for antibiotics. *FEMS Microbiol. Rev*. **41**, 653–671(2017).
4. Maynard, A., Butler, N., Ito, T., Silva, A., Murai, M., Chen, T., Koffas, M., Miyoshi, H., and Barquera, B. The antibiotic korormicin A kills bacteria by producing reactive oxygen species. *J. Bacteriol*. **201**, e00718–18 (2019).
5. Vohl, J. G., Casutt, M. S., Vorburger, T., Diederichs, K., and Fritz, G. Structure of the *V. cholerae* Na^+-pumping NADH:quinone oxidoreductase. *Nature* **516**, 62–67 (2014).
6. Hau, J-L., Kaltwasser, S., Muras, V., Casutt, M. S., Vohl, G., Claußen, B., Steffen, W., Leitner, A., Bill, E., Cutsail III, G. E., DeBeer, S., Vonck, J., Steuber, J., and Fritz, G. Conformational coupling of redox-driven Na^+-translocation in *Vibrio cholerae* NADH:quinone oxidoreductase. *Nat Struct Mol Biol*, **30**, 1685-1694 (2023).
7. Kishikawa, J., Ishikawa, M., Masuya, T., Murai, M., Kitazumi, Y., Butler, N. L., Kato, T., Barquera, B., and Miyoshi, H. Cryo-EM structures of Na^+-pumping NADH-ubiquinone oxidoreductase from *Vibrio cholerae*. *Nat. Commun.* **13**, 4082 (2022).
8. Barquera, B., Nilges, M. J., Morgan, J. E., Ramirez-Silva, L., Zhou, W., and Gennis, R. B. Mutagenesis study of the 2Fe-2S center and the FAD- binding site of the Na^+-translocating NADH:ubiquinone oxidoreductase from *Vibrio cholerae*. *Biochemistry* **43**, 12322–12330 (2004).
9. Turk, E., Puhar, A., Neese, F., Bill, E., Fritz, G., and Steuber, J. NADH oxidation by the Na^+-translocating NADH:quinone oxidoreductase from *Vibrio cholerae*: functional role of the NqrF subunit. *J. Biol. Chem.* **279,** 21349–21355 (2004).
10. Belevich, N. P., Bertsova, Y. V., Verkhovskaya, M. L., Baykov, A. A., and Bogachev A. V. Identification of the coupling step in Na^+-translocating NADH:quinone oxidoreductase from real-time kinetics of electron transfer. *Biochim. Biophys. Acta (Bioenerg.)* **1857**, 141–149 (2016).
11. Reyes-Prieto, A., Barquera, B., and Juárez, O. Origin and evolution of the sodium-pumping NADH: Ubiquinone oxidoreductase. *PLoS One* **9,** e96696 (2014).
12. Fadeeva, M. S., Bertsova, Y. V., Verkhovsky, M. I., and Bogachev, A. V. Site-directed mutagenesis of conserved cysteine residues in NqrD and NqrE subunits of Na^+-translocating NADH:quinone oxidoreductase. *Biochemistry* **73**, 123–129 (2008).

13. Hayashi, M., Nakayama, Y., Yasui, M., Maeda, M., Furuishi, K., and Unemoto, T. FMN is covalently attached to a threonine residue in the NqrB and NqrC subunits of Na^+-translocating NADH-quinone reductase from *Vibrio alginolyticus*. *FEBS Lett*. **488,** 5–8 (2001).
14. Barquera, B., Häse, C. C., and Gennis, R. B. Expression and mutagenesis of the NqrC subunit of the NQR respiratory Na^+ pump from *Vibrio cholerae* with covalently attached FMN. *FEBS Lett*. **492,** 45–49 (2001).
15. Juárez, O., Nilges, M. J., Gillespie, Cotton, P. J., and Barquera, B. Riboflavin is an active redox cofactor in the Na^+-pumping NADH: quinone oxidoreductase (Na^+-NQR) from *Vibrio cholerae. J. Biol. Chem*. **283,** 33162–33167 (2008).
16. Casutt, M. S., Huber, T., Brunisholz, R., Tao, M., Fritz, G., and Steuber, J. Localization and function of the membrane-bound riboflavin in the Na^+-translocating NADH:quinone oxidoreductase (Na^+-NQR) from *Vibrio cholerae. J. Biol. Chem*. **285,** 27088–27099 (2010).
17. Ishikawa, M., Masuya, T., Tanaka, H., Aoki, W., Hantman, N., Butler, N. L., Murai, M., Barquera, B., and Miyoshi, H. Specific chemical modification explores dynamic structure of the NqrB subunit in Na^+-pumping NADH-ubiquinone oxidoreductase from *Vibrio cholerae*. *Biochim. Biophys. Acta (Bioenergetics)*, **1862**, 148432 (2021).
18. Ishikawa, M., Masuya, T., Kuroda, S., Uno, S., Butler, N. L., Foreman, S., Murai, M., Barquera, B., and Miyoshi, H. The side chain of ubiquinone plays a critical role in Na^+ translocation by the NADH-ubiquinone oxidoreductase (Na^+-NQR) from *Vibrio cholerae*. *Biochim. Biophys. Acta (Bioenergetics)* **1863**, 148547 (2022).
19. Juárez, O., Morgan, J. E., and Barquera, B. The electron transfer pathway of the Na^+-pumping NADH: quinone oxidoreductase from *Vibrio cholerae*. *J. Biol. Chem*. **284**, 8963–8972 (2009). (23)
20. Juárez, O., Morgan, J. E., Nilges, M. J., and Barquera, B. Energy transducing redox steps of the Na^+-pumping NADH:quinone oxidoreductase from *Vibrio cholerae*. *Proc. Natl. Acad. Sci. USA* **107**, 12505—12510 (2010).
21. Bogachev, A. V., Belevich, N. P., Bertsova, Y. V., and Verkhovsky, M. I. Primary steps of the Na^+-translocating NADH:ubiquinone oxidoreductase catalytic cycle resolved by the ultrafast freeze-quench approach. *J. Biol. Chem*. **284**, 5533–5538 (2009).
22. Bogachev, A. V., Kulik, L. V., Bloch, D. A., Bertsova, Y. V., Fadeeva, M. S., and Verkhovsky, M. I. Redox properties of the prosthetic groups of Na^+-translocating NADH:quinone oxidoreductase. 1. Electron paramagnetic resonance study of the enzyme. *Biochemistry* **48,** 6291– 6298 (2009).
23. Barquera, B., Morgan, J. E., Lukoyanov, D., Scholes, C. P., Gennis, R. B., and Nilges, M. J. X- and W-band EPR and Q-band ENDOR studies of the flavin radical in the Na^+- translocating NADH:UQ oxidoreductase from *Vibrio cholerae*. *J. Am. Chem. Soc*. **125**, 265–275 (2003).
24. Tuz, K., Mezic, K. G., Xu, T., Barquera, B., and Juárez, O. The kinetic reaction mechanism of the *Vibrio cholerae* sodium-dependent NADH dehydrogenase. *J. Biol. Chem*. **290**, 20009–20021 (2015).

25. Page, C. C., Moser, C. C., Chen, X., and Dutton, P. L. Natural engineering principles of electron tunneling in biological oxidation-reduction. *Nature* **402**, 47–52 (1999).
26. Juárez, O., Athearn, K., Gillespie, P., and Barquera, B. Acid residues in the transmembrane helices of the Na^+-pumping NADH:quinone oxidoreductase from *Vibrio cholerae* involved in sodium translocation. *Biochemistry* **48**, 9516–9524 (2009).
27. Kumar, A., Roth, J., Kim, H., Saura, P., Bohn, S., Reif-Trauttmansdorff, Schubert, T., A., Kaila, V. R. I., Schuller, J. M., and Müller, V. Molecular principles of redox-coupled sodium pumping of the ancient Rnf machinery. *Nat. Commun*. **16**, 2302 (2024).
28. Ishikawa-Fukuda, M., Kishikawa, J., Masuya, T., Ito, T., Butler, N. L., McFee, D., Kato, T., Barquera, B., Miyoshi, H., and Murai, M. Structural elucidation of the mechanism for inhibitor resistance in the Na^+-translocating NADH-ubiquinone oxidoreductase from *Vibrio cholerae*. *Biochemistry* **64.** 9 (2025).
29. Punjani, A., Rubinstein, J. L., Fleet, D. J., and Brubaker, M. A. cryoSPARC: algorithms for rapid unsupervised cryo-EM structure determination. *Nat. Methods* **14**, 290–296 (2017).
30. Punjani, A., and Fleet, D. J. 3D variability analysis: Resolving continuous flexibility and discrete heterogeneity from single particle cryo-EM. *J. Struct. Biol.* **20**, 860-870 (2021).
31. Punjani, A., and Fleet, D. J. 3DFlex: determining structure and motion of flexible proteins from cryo-EM. *Nat. Meth.* **20**, 860-870 (2023).
32. Nakayama, Y., Yasui, M., Sugahara, K., Hayashi, M., and Unemoto, T. Covalently bound flavin in the NqrB and NqrC subunits of Na^+-translocating NADH-quinone reductase from *Vibrio alginolyticus*. *FEBS Lett*. **474**, 165–168 (2010).
33. Casutt, M. S., Schlosser, A., Buckel, W., and Steuber, J. The single NqrB and NqrC subunits in the Na^+-translocating NADH:quinone oxidoreductase (Na^+-NQR) from *Vibrio cholerae* each carry one covalently attached FMN. *Biochim. Biophys. Acta (Bioenerg.)* **1817**, 1817–1822 (2012).
34. Yoshikawa, K., Takadera, T., Adachi, K., Nishijima, M., and Sano, H. Korormicin, a novel antibiotic specifically active against marine gram-negative bacteria, produced by a marine bacterium. *J Antibiot (Tokyo)* **50**, 949–953 (1997).
35. Yoshikawa, K., Nakayama, Y., Hayashi, M., Unemoto, T., and Mochida, K. Korormicin, an antibiotic specific for gram-negative marine bacteria, strongly inhibits the respiratory chain-linked Na^+-translcoating NADH: quinone oxidoreductase from the marine *Vibrio alginolyticus. J Antibiot (Tokyo)* **52**, 182–185 (1999).
36. Nakayama, Y., Hayashi, M., Yoshikawa, K., Mochida, K., and Unemoto, T. Inhibitor studies of a new antibiotic, korormicin, 2-*n*-heptyl-4-hydroxyquinoline *N*-oxide and Ag^+ toward the Na^+-translocating NADH-quinone reductase from the marine *Vibrio alginolyticus*. *Biol. Pharm. Bull.* **22**, 1064–1067 (1999).

37. Uehara, H., Oishi, T., Yoshikawa, K., Mochida, K., and Hirama, M. The absolute configuration and total synthesis of korormicin. *Tetrahedron Lett.* **40**, 8641–8645 (1999).
38. Hayashi, M., Shibata, N., Nakayama, Y., Yoshikawa, K., and Unemoto, T. Korormicin insensitivity in *Vibrio alginolyticus* is correlated with a single point mutation of Gly-140 in the NqrB subunit of the Na^+-translocating NADH-quinone reductase. *Arch. Biochem. Biophys.* **401**, 173–177 (2002).
39. Tebben, J., Motti, C., Tapiolas, D., Thomas-Hall, P., and Harder, T. A coralline algal-associated bacterium, *Pseudoalteromonas* strain J010, yields five new korormicins and a bromopyrrole. *Mar Drugs* **12**, 2802–2815 (2014).
40. Ito, T., Murai, M., Ninokura, S., Kitazumi, Y., Mezic, K. G., Cress, B. F., Koffas, M. A. G., Morgan, J. E., Barquera, B., and Miyoshi, H. Identification of the binding sites for UQ and inhibitors in the Na^+-pumping NADH-UQ oxidoreductase of *Vibrio cholerae* by photoaffinity labeling. *J. Biol. Chem*. **292**, 7727–7742 (2017).
41. Schlitter, J., Engels, M., and Krüger, P. Targeted molecular dynamics: A new approach for searching pathways of conformational transitions. *J. Mol. Graphics*. **12**, 2, 84-89 (1994).
42. Okazaki, K., Wöhlert, D., Warnau, J., Jung, H., Yildiz, Ö., Kühlbrandt, W., and Hummer, G. Mechanism of the electroneutral sodium/proton antiporter PaNhaP from transition-path shooting. *Nat. Commun.* **10**, 1742 (2019).
43. Bright, J. N., Shrivastava, I. H., Cordes, F. S., and Sansom, M. S. Conformational dynamics of helix S6 from Shaker potassium channel: simulation studies. *Biopolymers*. **64**, 6, 303-13 (2002).
44. Schägger, H. Tricine-SDS-PAGE. *Nat. Protoc*., **1**, 16-22 (2006).
45. Emsley, P., Lohkamp, B., Scott, W. G., and Cowtan, K. Features and development of Coot. *Acta Crystallogr. D. Biol. Crystallogr*. **66**, 486–501 (2010).
46. Liebschner, D., Afonine, P. V., Baker, M. L., Bunkóczi, G., Chen, V. B., Croll, T. I., Hintze, B., Hung, L. W., Jain, S., McCoy, A. J., Moriarty, N. W., Oeffner, R. D., Poon, B. K., Prisant, M. G., Read, R. J., Richardson, J. S., Richardson, D. C., Sammito, M. D., Sobolev, O. V., Stockwell, D. H., Terwilliger, T. C., Urzhumtsev, A. G., Videau, L. L., Williams, C. J., and Adams, P. D. Macromolecular structure determination using X-rays, neutrons and electrons: recent developments in Phenix. *Acta Crystallogr. D. Struct. Biol*. **75**, 861–877 (2019).
47. Chen, V. B., Arendall, W. B., Headd, J. J., Keedy, D. A., Immormino, R. M., Kapral, G. J., Murray, L. W., Richardson, J. S., and Richardson, D. C. MolProbity: all-atom structure validation for macromolecular crystallography. *Acta Crystallogr. D. Biol. Crystallogr.* **66**, 12–21 (2010).
48. Pettersen, E. F., Goddard, T. D., Huang, C. C., Meng, E. C., Couch, G. S., Croll, T. I., Morris, J. H., and Ferrin, T. E. UCSF ChimeraX: Structure visualization for researchers, educators, and developers. *Protein Sci*. **30**, 70–82 (2021).
49. Coutsias, E. A., Seok, C., Jacobson, M. P., and Dill, K. A. A. Kinematic view of loop closure. *J.*

Comput. Chem. **25**, 510 (2004).

50. Jo, S., Kim, T., Iyer, V. G., and Im, W. CHARMM-GUI: a web-based graphical user interface for CHARMM. *J. Comput. Chem.* **29**, 1859－1865 (2008).
51. Wu, E. L., Cheng, X., Jo, S., Rui, H., Song, K. C., Dávila-Contreras, E. M., Qi, Y., Lee, J., Monje-Galvan, V., Venable, R. M., Klauda, J. B., and Im, W. CHARMM-GUI membrane builder toward realistic biological membrane simulations. *J. Comput. Chem.* **35**, 1997－2004 (2014).
52. Best, R. B., Zhu, X., Shim, J., Lopes, P. E. M., Mittai, J., Feig, M., and MacKerell Jr, A. D. Optimization of the additive CHARMM all-atom protein force field targeting improved sampling of the backbone ϕ, ψ and side-chain χ1 and χ2 dihedral angles. *J. Chem*. *Theory Comput.* **8**, 3257 (2012).
53. Gamiz-Hernandez, A. P., Jussupow, A., Johansson, M. P., and Kaila, V. R. I. Terminal electron–proton transfer dynamics in the quinone reduction of respiratory complex I. *J. Am. Chem. Soc*. **139**, 16282–16288 (2017).
54. Di Luca, A., Gamiz-Hernandez, A. P., and Kaila, V. R. I. Symmetry-related proton transfer pathways in respiratory complex I. *Proc Natl Acad Sci U S A*.**114**, 31, E6314-E6321 (2017).
55. Darden, T., York, D., and Pedersen, L. Particle mesh Ewald: An *N*·log(*N*) method for Ewald Sums in large systems. *J. Chem. Phys*. **98**, 10089 (1993).
56. Loncharich, R. J., Brooks, B. R., and Pastor, R. W. Langevin dynamics of peptides: the frictional dependence of isomerization rates of *N*-acetylalanyl-*N*'-methylamide. *Biopolymers*, **32**, 523 (1992).
57. Martyna, G. J., Tobias, D. J., and Klein, M. L. Constant pressure molecular dynamics algorithms. *J. Chem. Phys*. **101**, 4177 (1994).
58. Feller, S. WE., Zhang, Y., Pastor, R. W., and Brooks, B. R. Constant pressure molecular dynamics simulation: The Langevin piston method. *J. Chem. Phys*. **103**, 4613 (1995).
59. Ryckaert, J. P., Ciccotti, G., and Berendsen, H. J. C. Numerical integration of the Cartesian equations of motion of a system with constraints: molecular dynamics of *n*-Alkanes. *J. Comput. Phys*. **23**, 327 (1977).
60. Phillips, J. C., Hardy, D. J., Maia, J. D. C., Stone, J. E., Ribeiro, J. V., Bernardi, R. C., Buch, R., Fiorin, G., Hénin, J., Jian, W., McGreevy, R., Melo, M. C. R., Radak, B. K., Skeel, R. D., Singharoy, A., Wang, Y., Roux, B., Chipot, C., and Tajkhorshid, E. Scalable molecular dynamics on CPU and GPU architectures with NAMD. *J. Chem. Phys*. **153**, 044130 (2020).

535

536

537 **FIGURES AND LEGENDS (for Main Figures)**

538

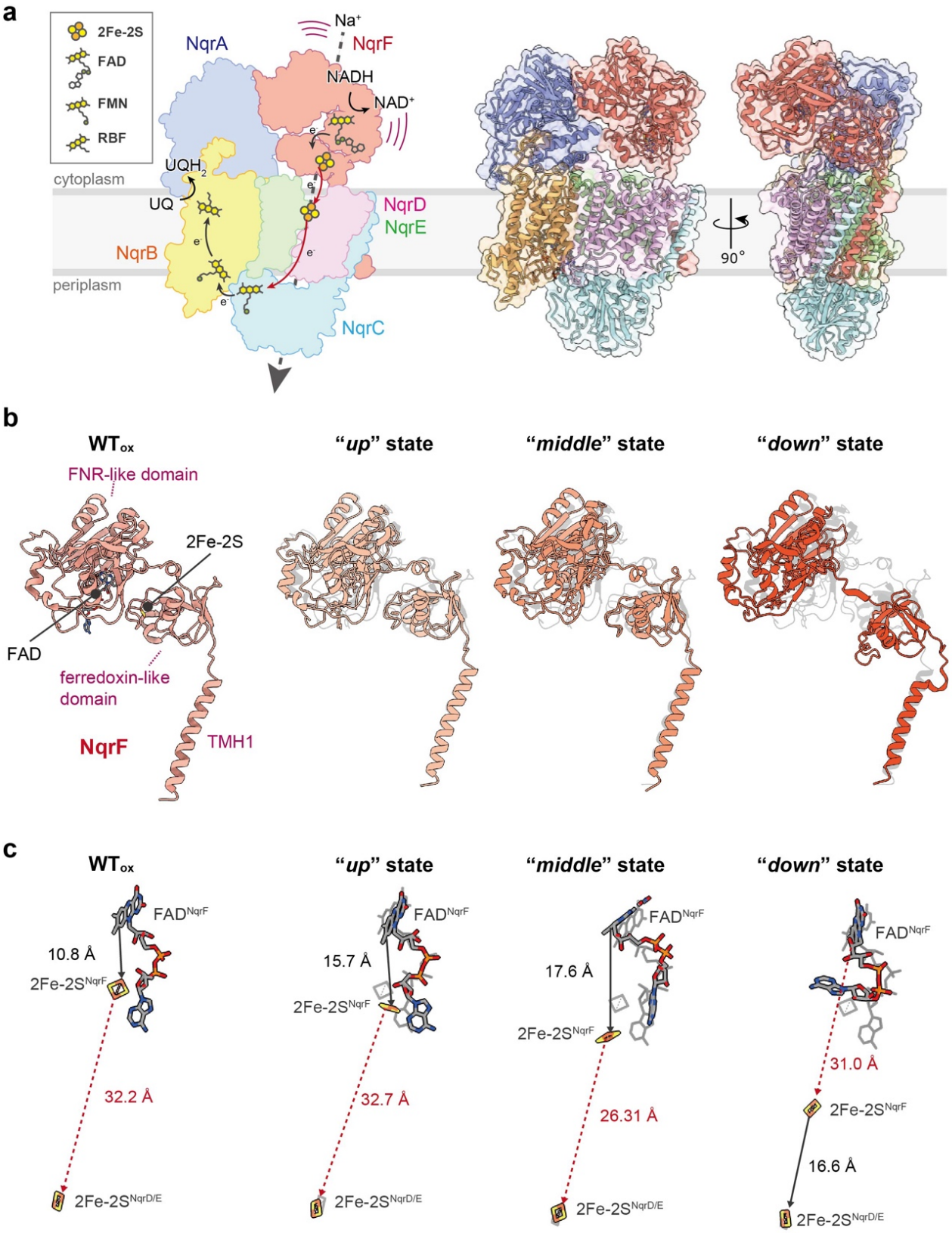

539 **Fig. 1 (continued)**

540

541 **Fig. 1: Architecture of Na^+-NQR.** ***a,*** Location of redox cofactors and electron transfer steps in the
542 overall architecture of Na+-NQR (**WT_{ox}**: pdb: 7XK3). *Left* hand panel: simplified structure of Na^+-NQR
543 showing the locations of redox cofactors and depicting electron transfer steps as arrows. Distances
544 consistent with electron transfer are colored in *gray,* whereas long distances in this structural
545 conformation, inconsistent with electron transfer ($2Fe\text{-}2S^{NqrF} \rightarrow 2Fe\text{-}2S^{NqrD/E}$, $2Fe\text{-}2S^{NqrD/E} \rightarrow FMN^{NqrC}$),
546 are colored in *red*. *Middle* and *right*-hand panels: the Na^+-NQR assembly from front and side views,
547 respectively. ***b,*** The "***up***", "***middle***", and "***down***" conformational states: The *left* panel shows the FNR
548 domain containing the FAD cofactor, ferredoxin-like domain containing 2Fe-2S, and TMH1 of NqrF
549 (side view). The remaining panels show the structure of NqrF in each conformational state illustrating
550 the pivotal motion of NqrF in **WT_{red}/ - Na^+**. To compare **WT_{ox}** and all states in **WT_{red}/- Na^+**, the images
551 of NqrF in **WT_{ox}** are shown as a *gray silhouette*. ***c,*** Changes in distances between cofactors that
552 accompany these conformational changes. The changes in distance between 2Fe-2S and FAD in NqrF,
553 **WT_{red}/ - Na^+**. For comparison of **WT_{ox}** with all states in **WT_{red}/- Na^+**, the relative locations of **WT_{ox}** are
554 overlapped as *gray silhouette*. *Black continuous arrows* indicate feasible distances for electron transfer,
555 and *red dashed arrows* indicate distances that are not consistent with electron transfer.
556

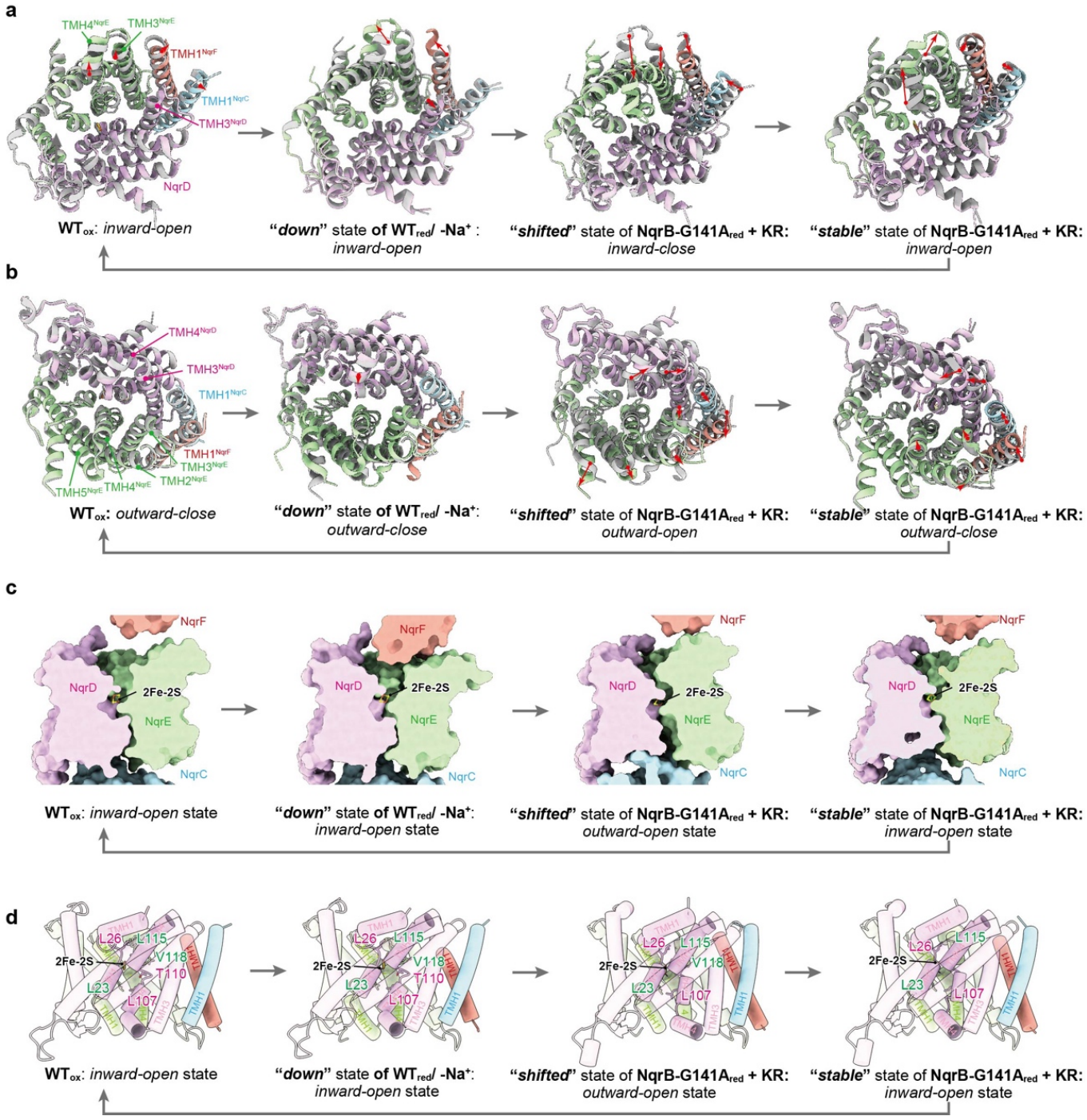

Fig. 2 (continued)

562 **Fig 2: Conformations of the transmembrane helices of NqrCDEF as the catalytic cycle progresses**
563 **from four different views.** Four steps in the catalytic cycle are represented by the following structures:
564 **WT_{ox}**, "***down***" state of **WT_{red}/ - Na^+**, "***shifted***" state, and "***stable***" state of **NqrB-G141A_{red} + KR**. *Gray*
565 images show the structure of the previous state; red arrows show the direction of movement from the
566 previous state to the current state. ***a,*** Cytoplasmic view. ***b,*** Periplasmic view. ***c,*** Sectional side views of
567 NqrCDEF. ***d,*** Tube models from front view. The critical amino acid residues to coordinate Na^+ in the
568 inward and outward gates in the MD simulation are shown as stick models. Supplementary Videos 2, 3,
569 and 4 show how the arrangement of the helices morphs during the catalytic cycle from the complete
570 view of the enzyme, cytoplasmic, and periplasmic views.
571

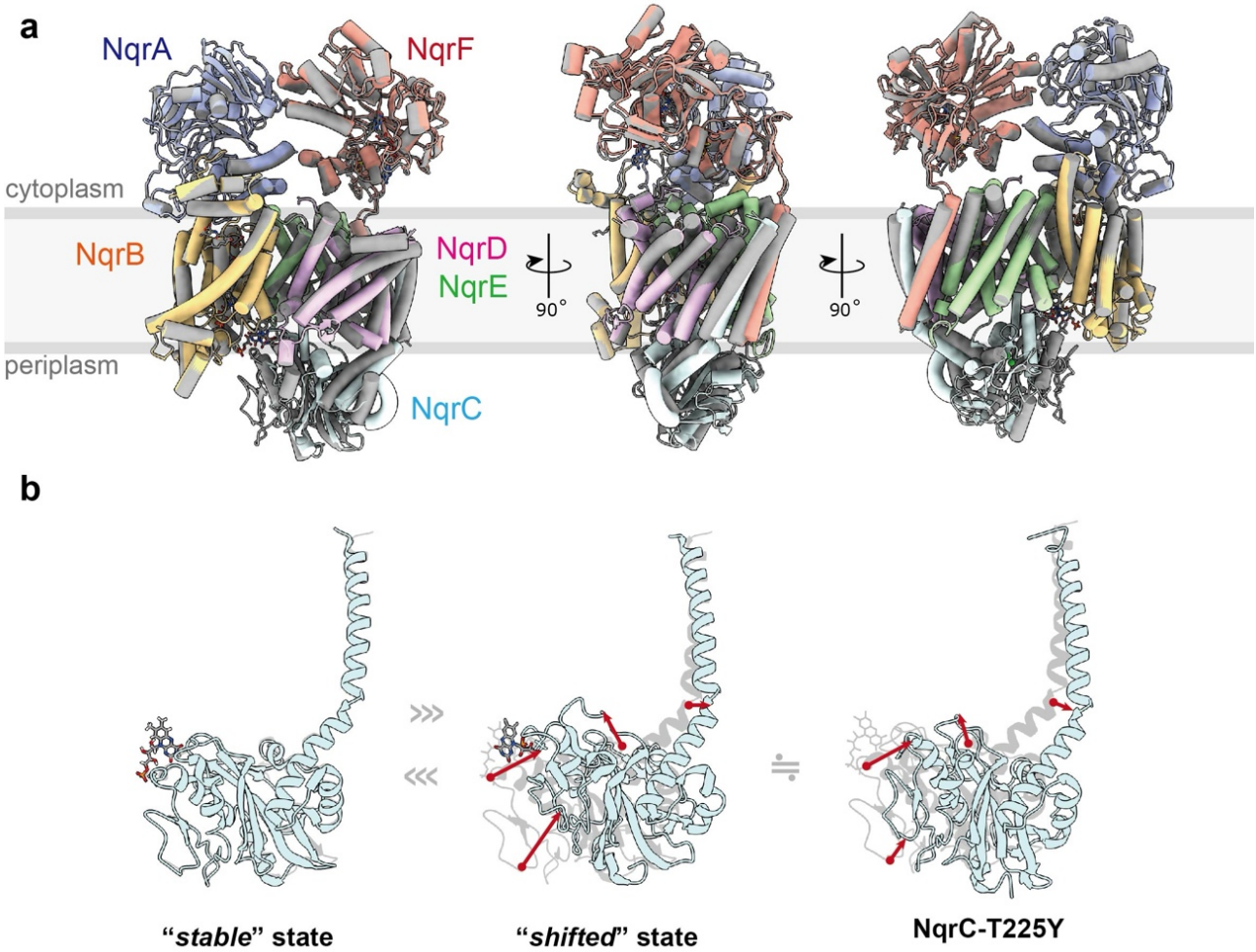

Fig. 3: The shift of NqrC: Transition of NqrC from "*stable*" to "*shifted*" conformation. *a,* Comparison of two states in **NqrB-G141A$_{red}$ + KR** sample, complete structure from three different views; "***stable***" state (*gray*) and "***shifted***" state (*color*). In the "***stable***" state (88% of particles) the hydrophilic region of NqrC is located close to NqrB; in the "***shifted***" state (12% of particles) NqrC is close to NqrD (Supplementary Fig. 1e). ***b,*** NqrC is shown alone. *Left*, "***stable***" state from **NqrB-G141A$_{red}$ + KR**; center, "***shifted***" state from **NqrB-G141A$_{red}$ + KR**; *right*, NqrC from **NqrC-T225Y$_{red}$**. For comparison, the *gray silhouettes* in the center and right-hand images show the "***stable***" state.

582

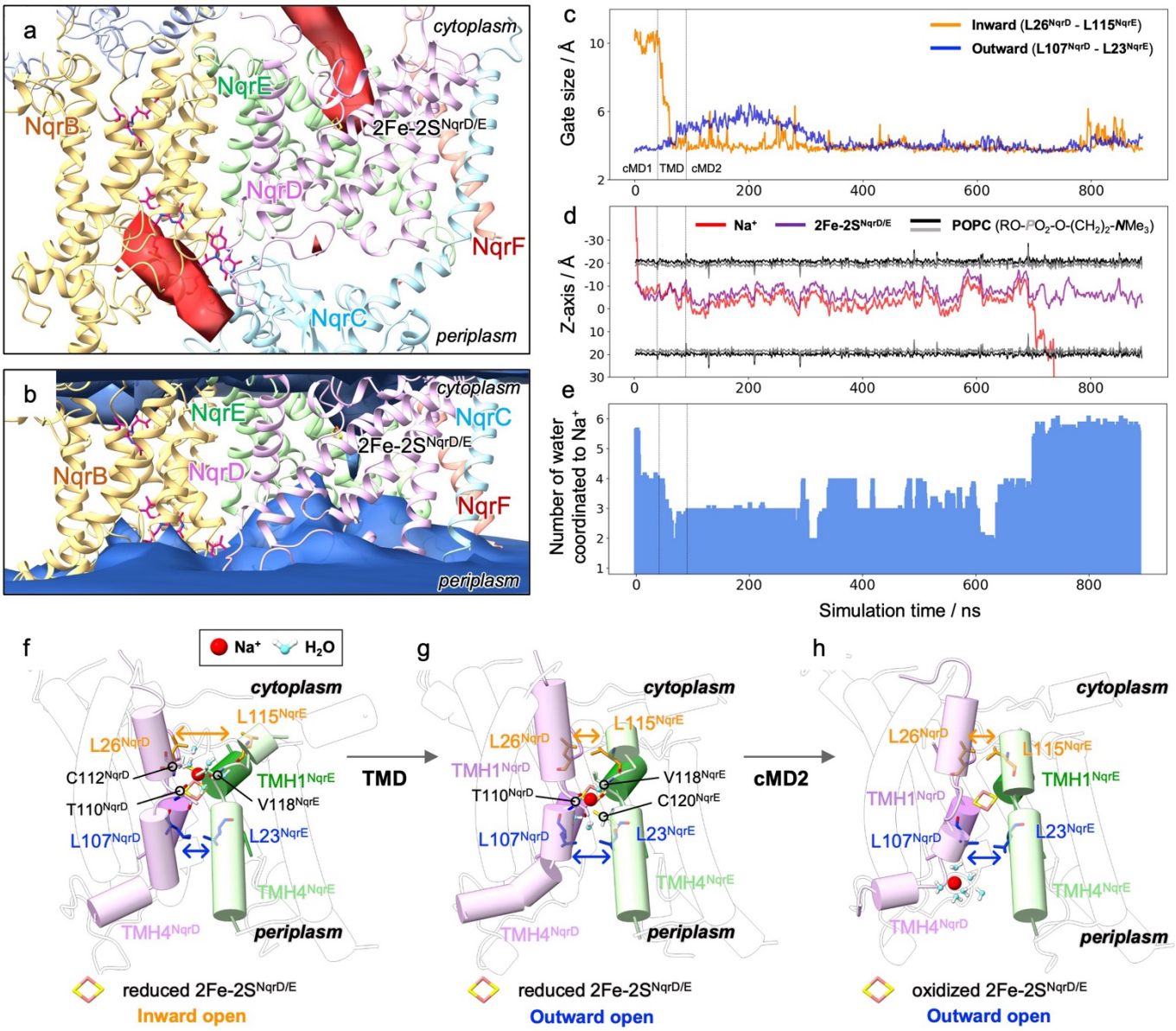

583

584

585

586 **Fig. 4 (continued)**

587

588 **Fig 4: Na^+ translocation pathway from MD simulation.** ***a-b,*** The accessibilities of Na^+ and water are
589 shown in the structure of wild-type of Na^+-NQR with reduced 2Fe-2S^{NqrF} and 2Fe-2S$^{NqrD/E}$. ***a,*** The spatial
590 density of Na^+ is shown in *red*; the relative iso-density surface of 3.5 to the bulk value is shown. ***b,*** The
591 spatial density of water is shown in *cyan*; the relative iso-density surface of 0.3 to the bulk value is
592 shown. ***c-e,*** A first conventional MD (cMD1) using the inward-open model containing reduced 2Fe-
593 2S^{NqrF} and 2Fe-2S$^{NqrD/E}$ based on $\mathbf{WT_{ox}}$ structure is followed by the targeted MD (TMD) inducing the
594 *inward-to-outward* transition of TMHs bundle and the second conventional MD (cMD2) containing
595 oxidized 2Fe-2Ss and reduced FMN^{NqrC}. ***c,*** The inward gate and outward gate size are defined by the
596 distances between L26^{NqrD} and L115^{NqrE} (*red*), and between L107^{NqrD} and L23^{NqrE} (*blue*), respectively.
597 The transitions of these gate sizes are shown during the simulation. ***d,*** The z coordinates (perpendicular
598 to the membrane surface) of the Na^+ being translocated and the 2Fe-2S$^{NqrD/E}$ are shown together with
599 the positions of the membrane positions. ***e,*** Number of water molecules coordinated to the Na^+ as a
600 function of time in the simulation. ***f-g,*** Representative snapshots during Na^+ translocation in MD
601 simulation. The amino acid residues that coordinate Na^+ ion in the inward and outward gates are
602 indicated in *red* and *blue* stick models, respectively. Na^+ bound in the inward-open and outward-open
603 conformations are shown in ***f*** and ***g***, respectively. The released of Na^+ to the periplasm is shown in ***h***.
604
605
606

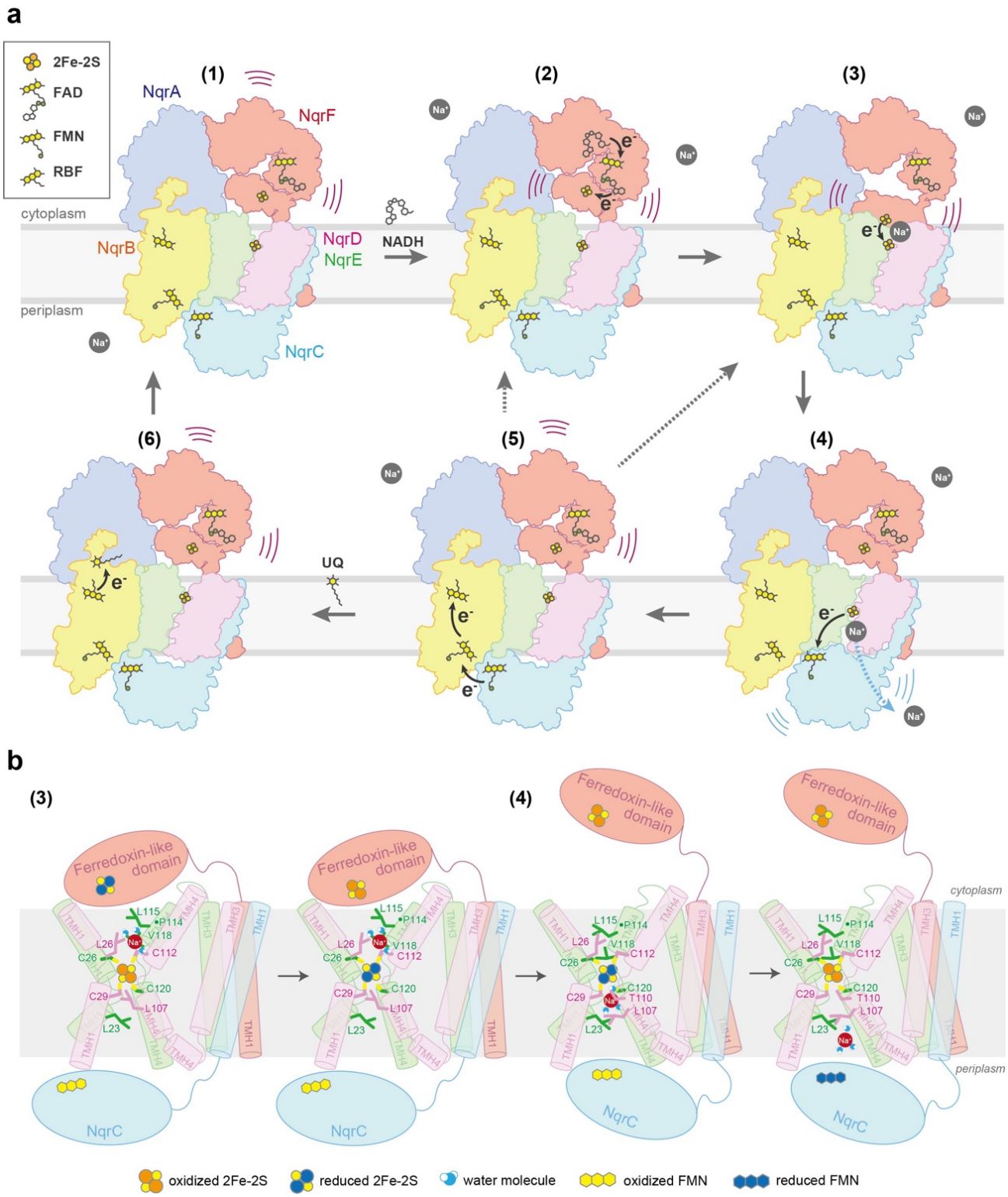

Fig. 5 (continued)

612 **Fig. 5: The model of conformational changes.** ***a,*** The cascade of conformational changes. One electron
613 flow is shown as *black arrows*. Step 1: oxidized state, step 2: NADH binding, step 3: Na^+ uptake, Step
614 4: transition to outward-open conformation, step 5: Na^+ release and return to inward-open conformation,
615 Step 6: UQ reduction. Since UQ requires a two-electron reduction, step 5 or 6 need to go back step 2 or
616 3. ***b,*** The detailed model of essential TMHs for conformational changes in step 3-4.
617
618

619 **Table 1: The list of samples for cryo-EM analysis.**

Sample name (PDB ID)	variant	NADH	inhibitor	Na^+	trait	$TMH^{NqrCDEF}$ conformation
WT_{red} (9UUU)	wild-type	+	−	+	−	Inward-opened
WT_{red}/ -Na^+ ***"up"* state (9UD6)** ***"middle"* state (9UD8)** ***"down"* state (9UD9)**	wild-type	+	−	−	−	Inward-opened (***all state***)
WT_{red} + KR (9UD5)	wild-type	+	KR	+	−	Inward-opened
WT_{red} + AD-42 (9UDG)	wild-type	+	AD-42	+	−	Inward-opened
NqrB-G141A_{red} + KR ***"stable"* state (9UDA)** ***"shifted"* state (9UDF)**	NqrB-G141A	+	KR	+	KR resistant	Inward-opened ("***stable" state***) Outward-opened ("***shifted" state***)
NqrB-T236Y_{ox} (9UD3)	NqrC-T225Y	−	−	+	FMN^{NqrB} missing	Inward-opened
NqrB-T236Y_{red} (9UD4)	NqrC-T225Y	+	−	+	FMN^{NqrB} missing	Inward-opened
NqrC-T225Y_{ox} (9U5G)	NqrC-T225Y	−	−	+	FMN^{NqrC} missing	Outward-opened
NqrC-T225Y_{red} (9UD2)	NqrC-T225Y	+	−	+	FMN^{NqrC} missing	Outward-opened

620
621
622
623
624

625 **EXTENDED DATA FIGURES**

626

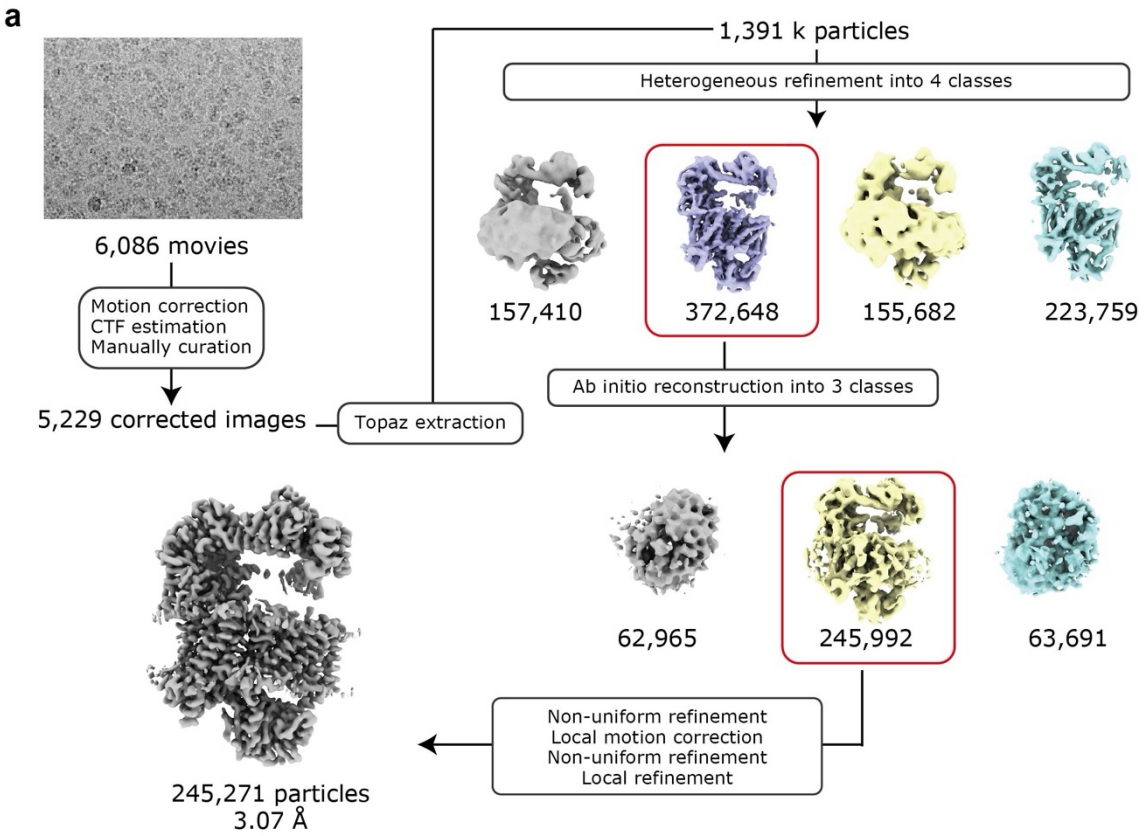

627

628

629

630 **Extended Data Fig. 1 (continued)**

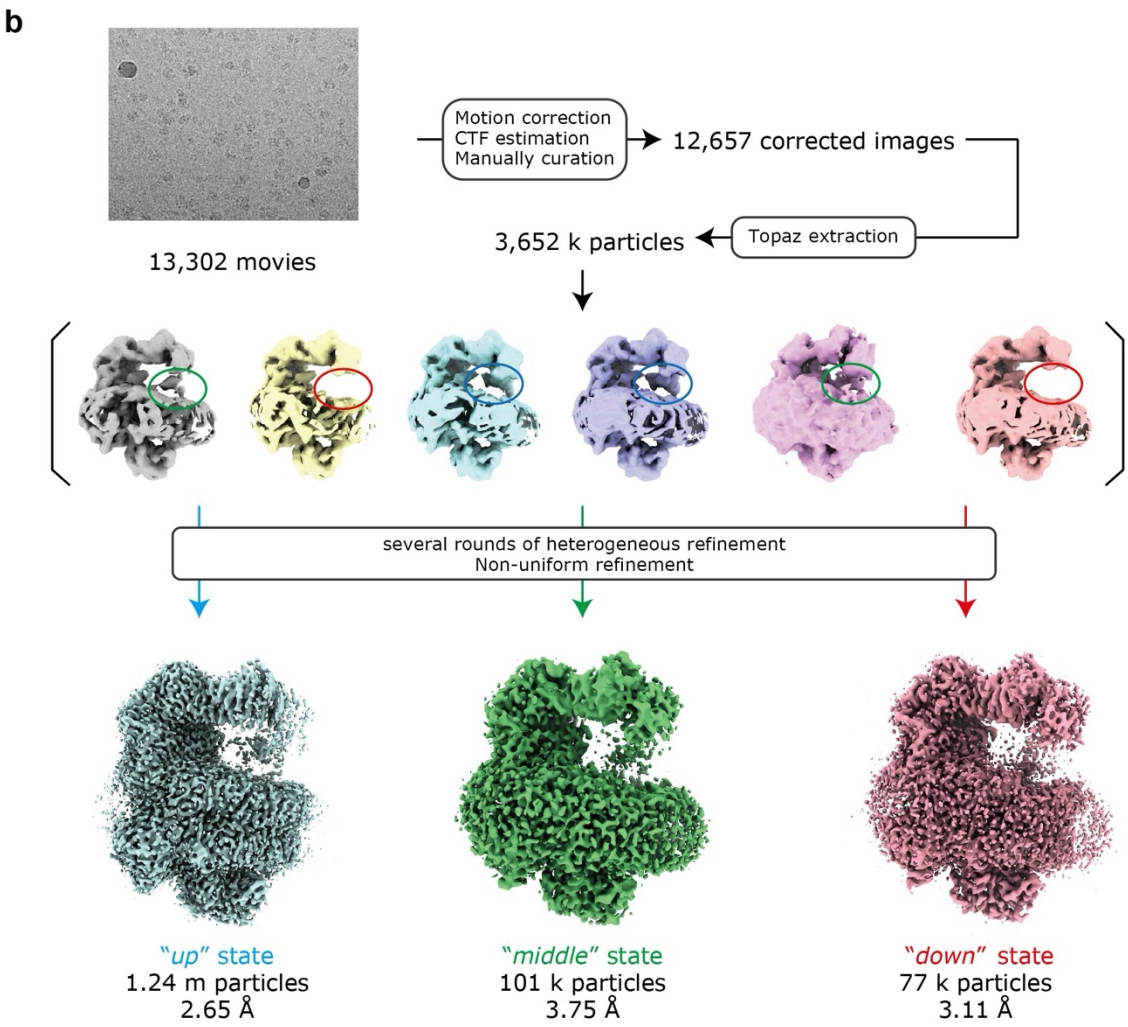

Extended Data Fig. 1 (continued)

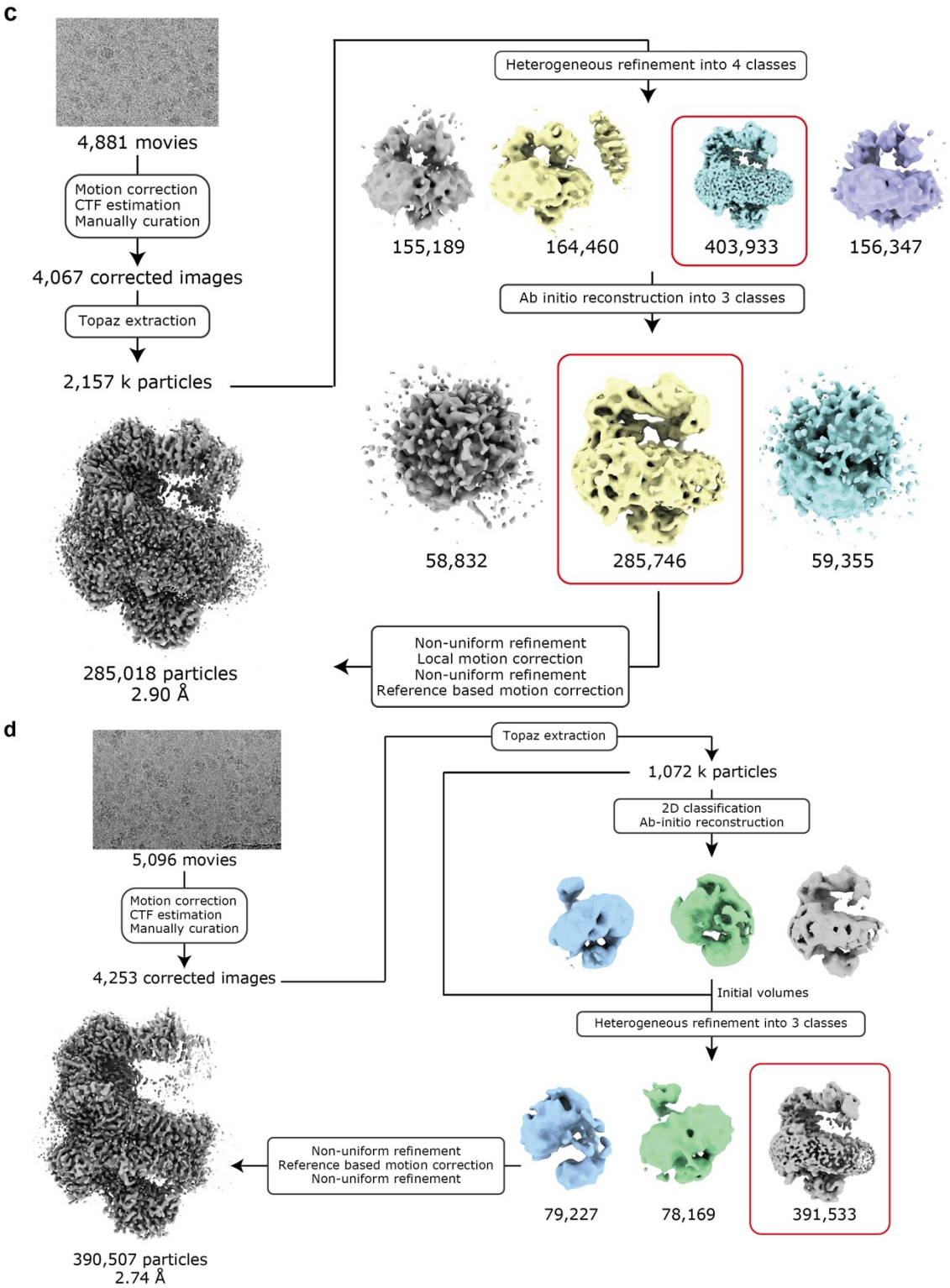

Extended Data Fig. 1 (continued)

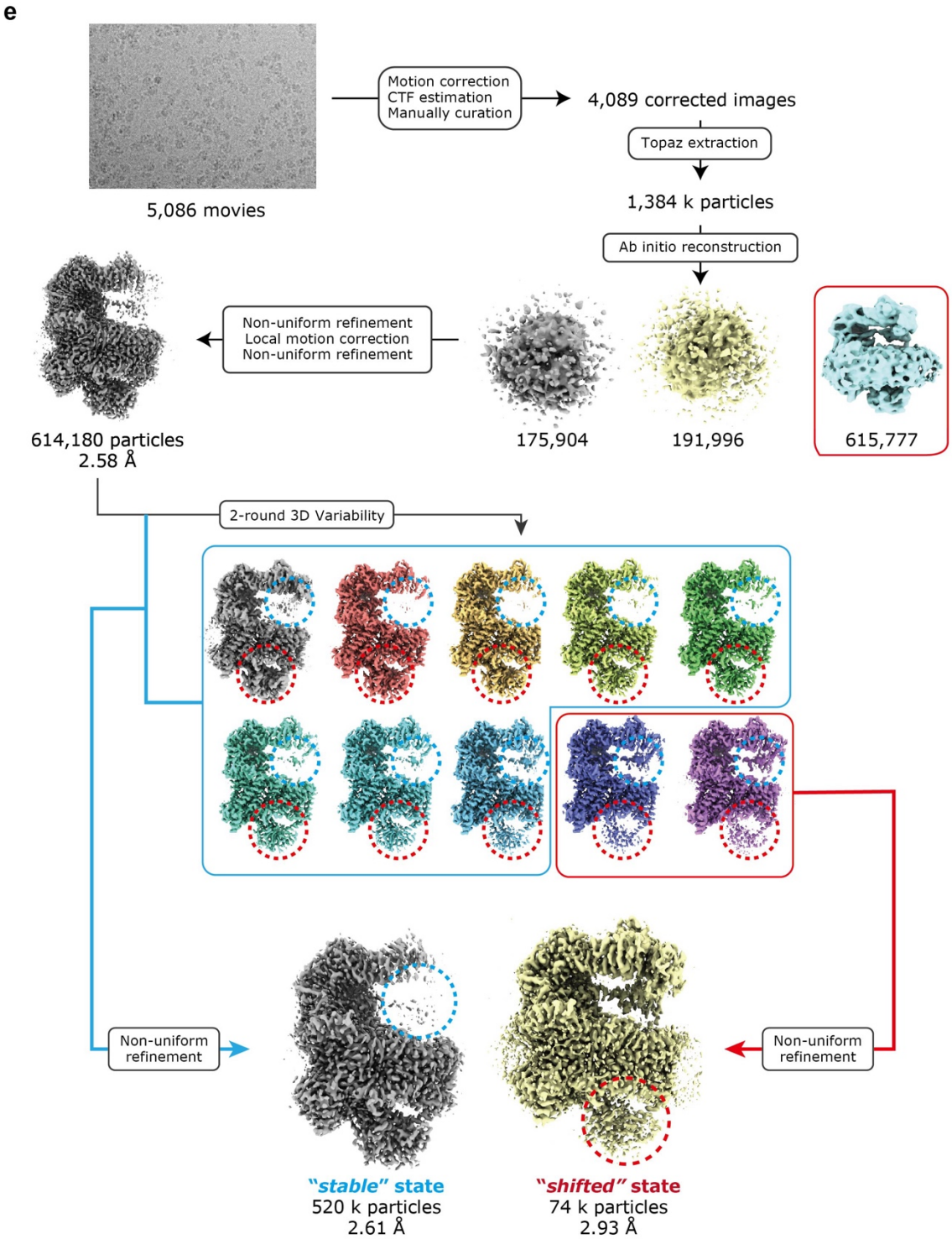

640

641

642 **Extended Data Fig. 1 (continued)**

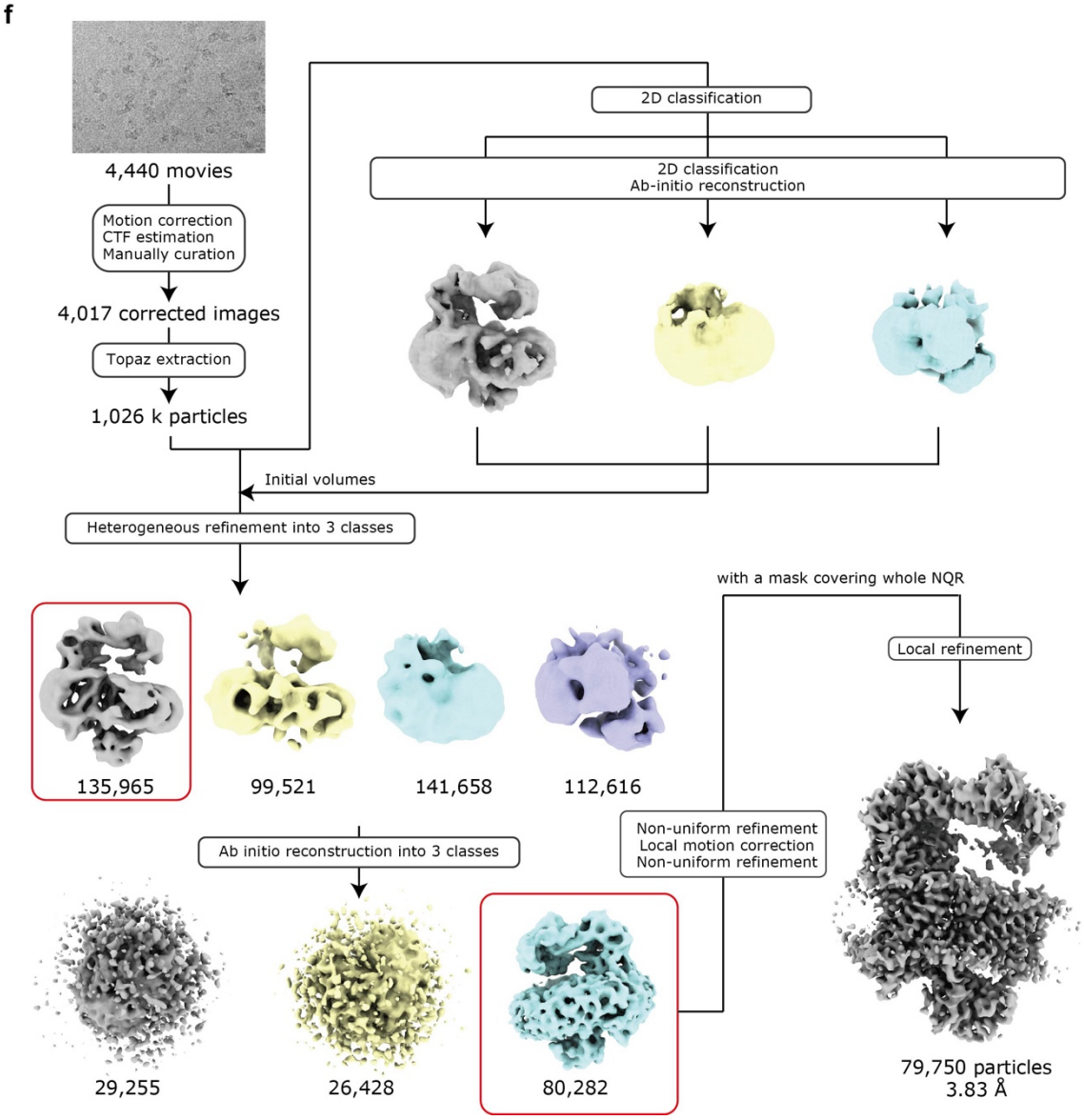

Extended Data Fig. 1 (continued)

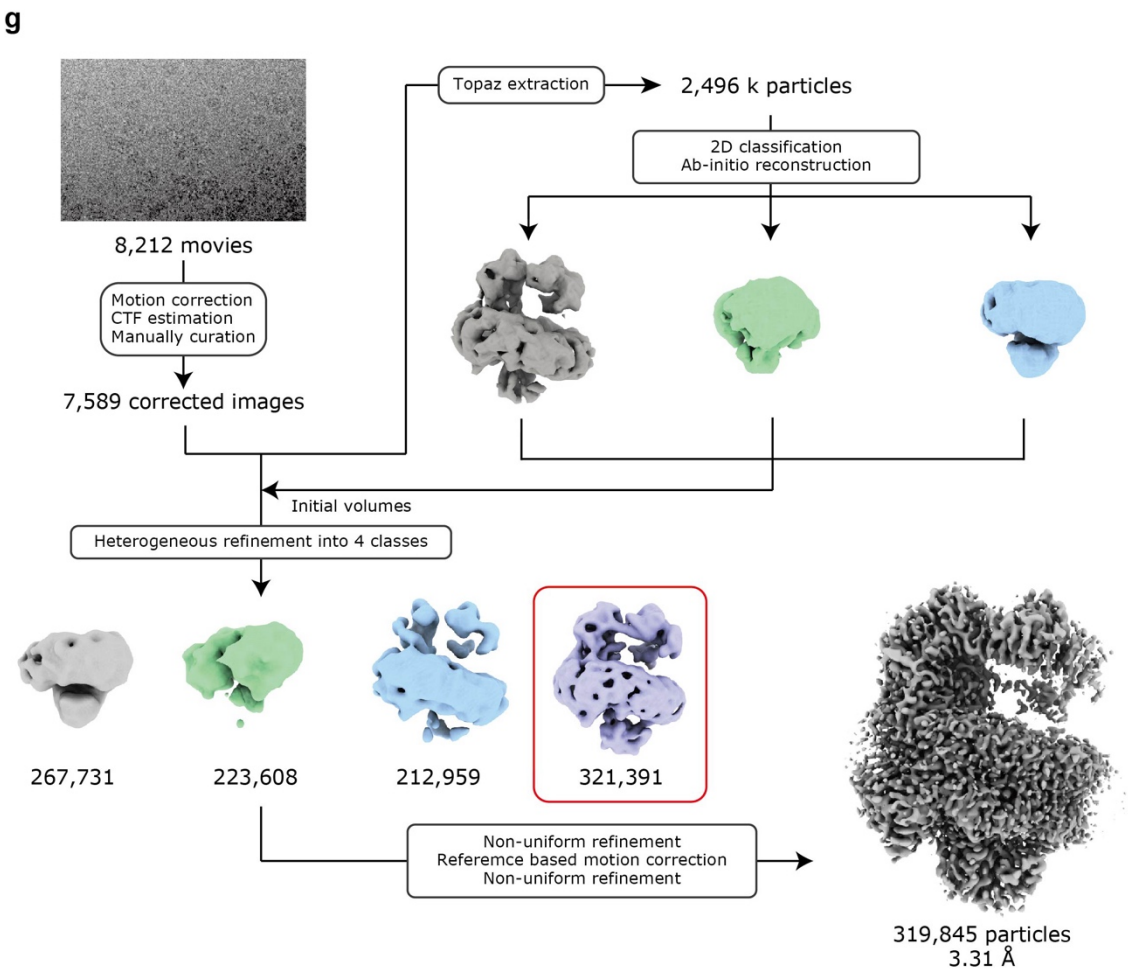

Extended Data Fig. 1 (continued)

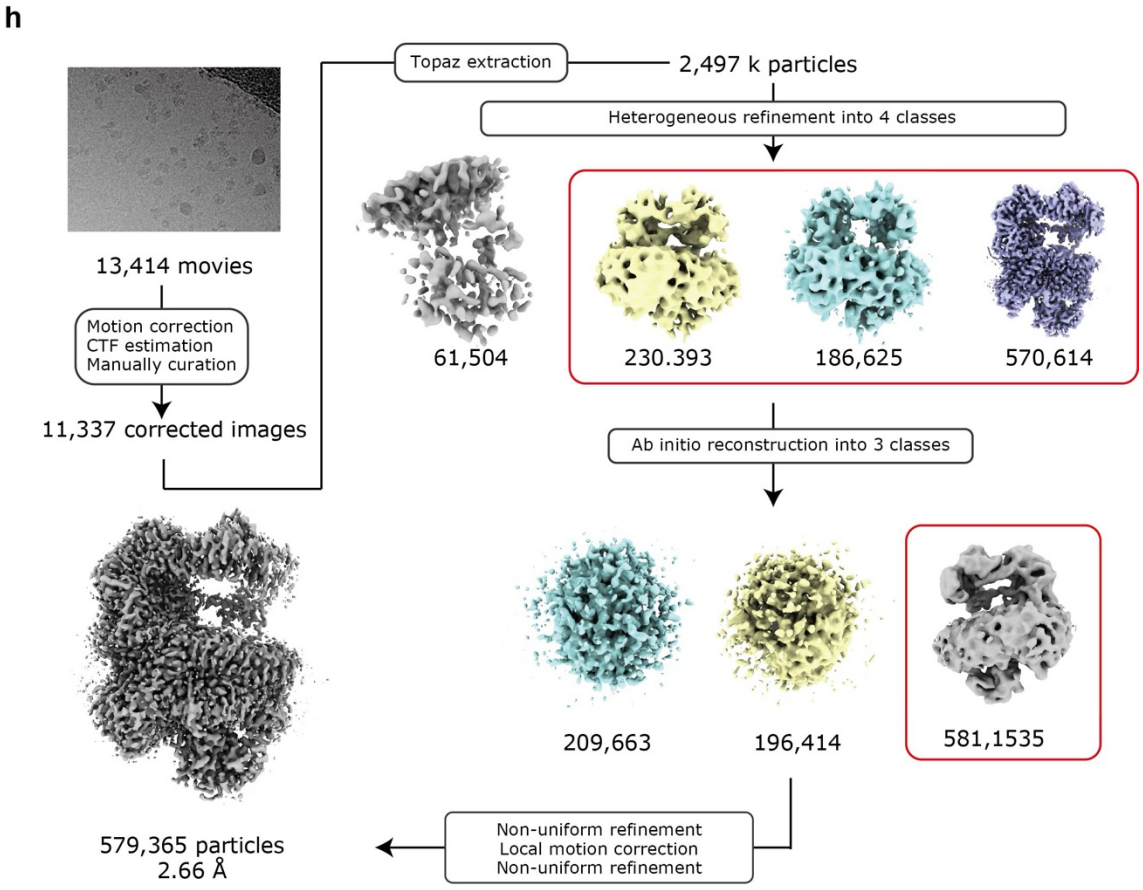

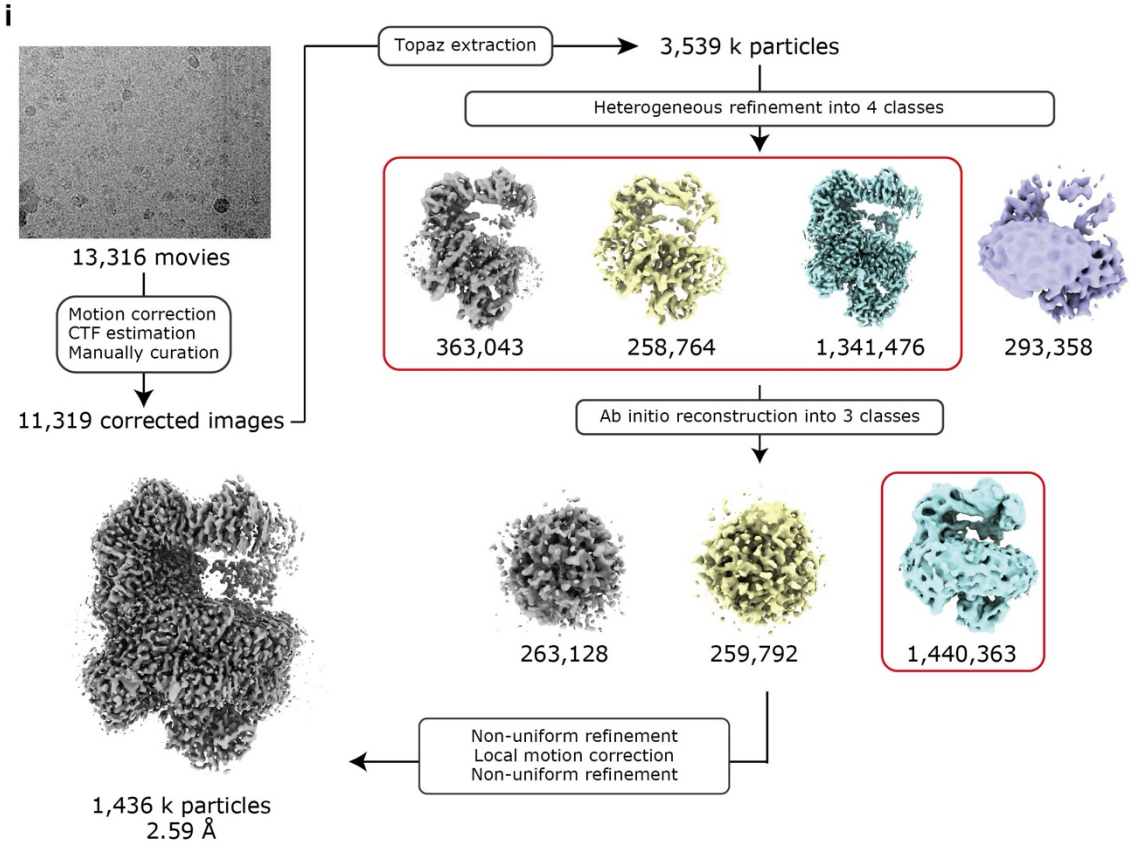

Extended Data Fig. 1 (continued)

Extended Data Fig. 1: The scheme of single particle analysis with cryoSPARC. *a:* WT_{red}, *b:* WT_{red}/-Na^+, *c:* WT_{red} + KR, *d:* WT_{red} + AD-42, *e:* NqrB-$G141A_{red}$ + KR, *f:* NqrB-$T236Y_{ox}$, *g:* NqrB-$T236Y_{red}$, *h:* NqrC-$T225Y_{ox}$, *i:* NqrC-$T225Y_{red}$. The classes surrounded by *red squares* were used in the next step. In ***e***, *red* and *blue circles* indicate the hydrophilic domain of NqrC and the ferredoxin-like domain of NqrF, respectively. The image processing for each dataset was implemented following each flow chart.

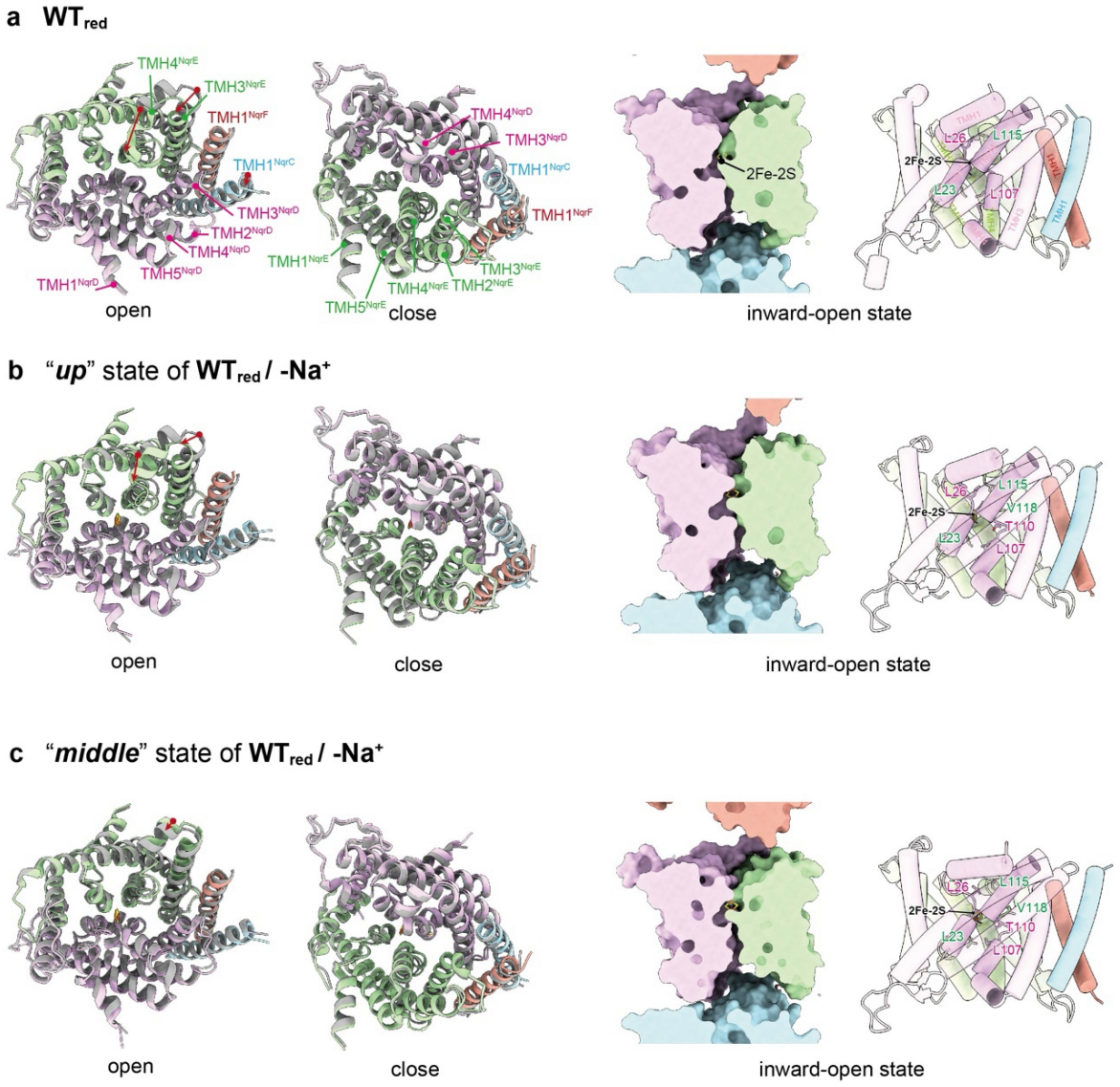

Extended Data Fig. 2 (continued)

667

d NqrB-T236Y$_{ox}$

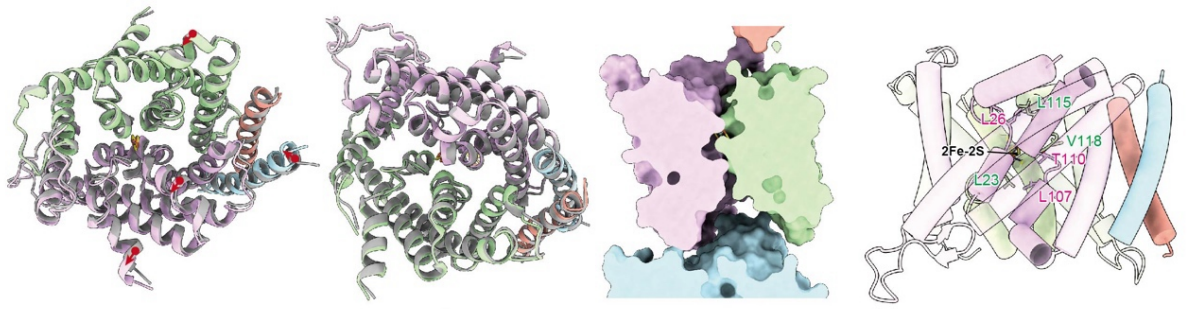

open close inward-open state

e NqrB-T236Y$_{red}$

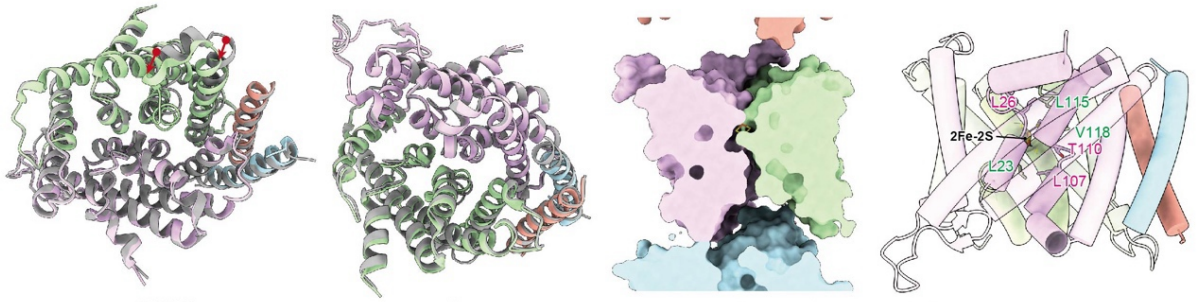

open close inward-open state

f NqrC-T225Y$_{ox}$

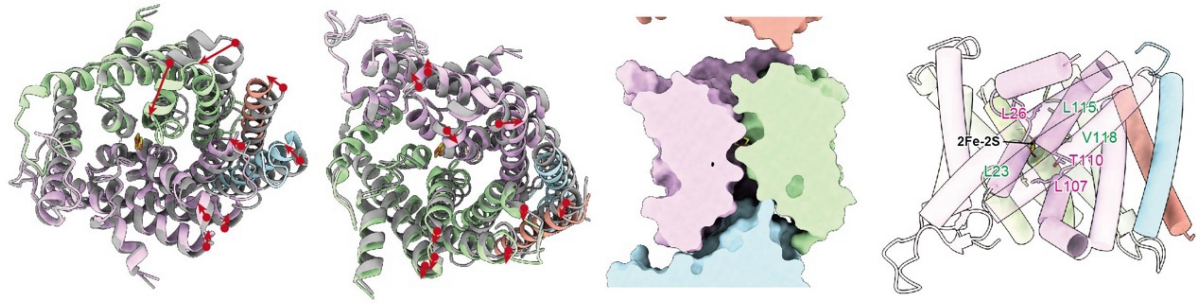

close open outward-open state

g NqrC-T225Y$_{red}$

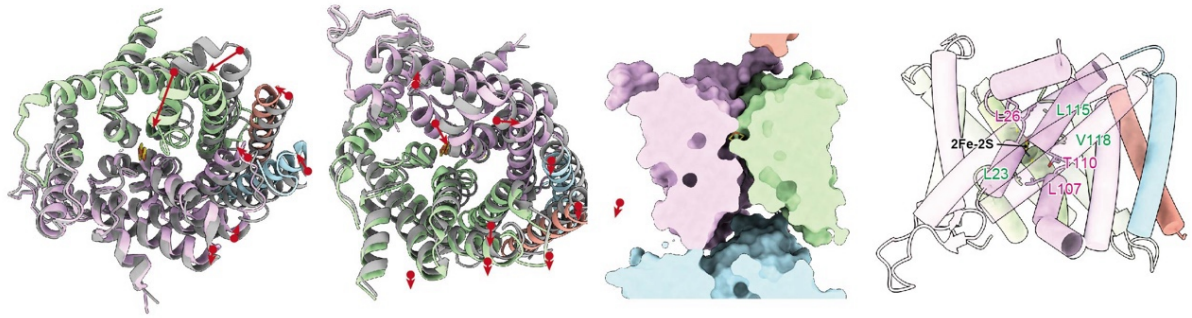

668 close open outward-open state

669

670 **Extended Data Fig. 2 (continued)**

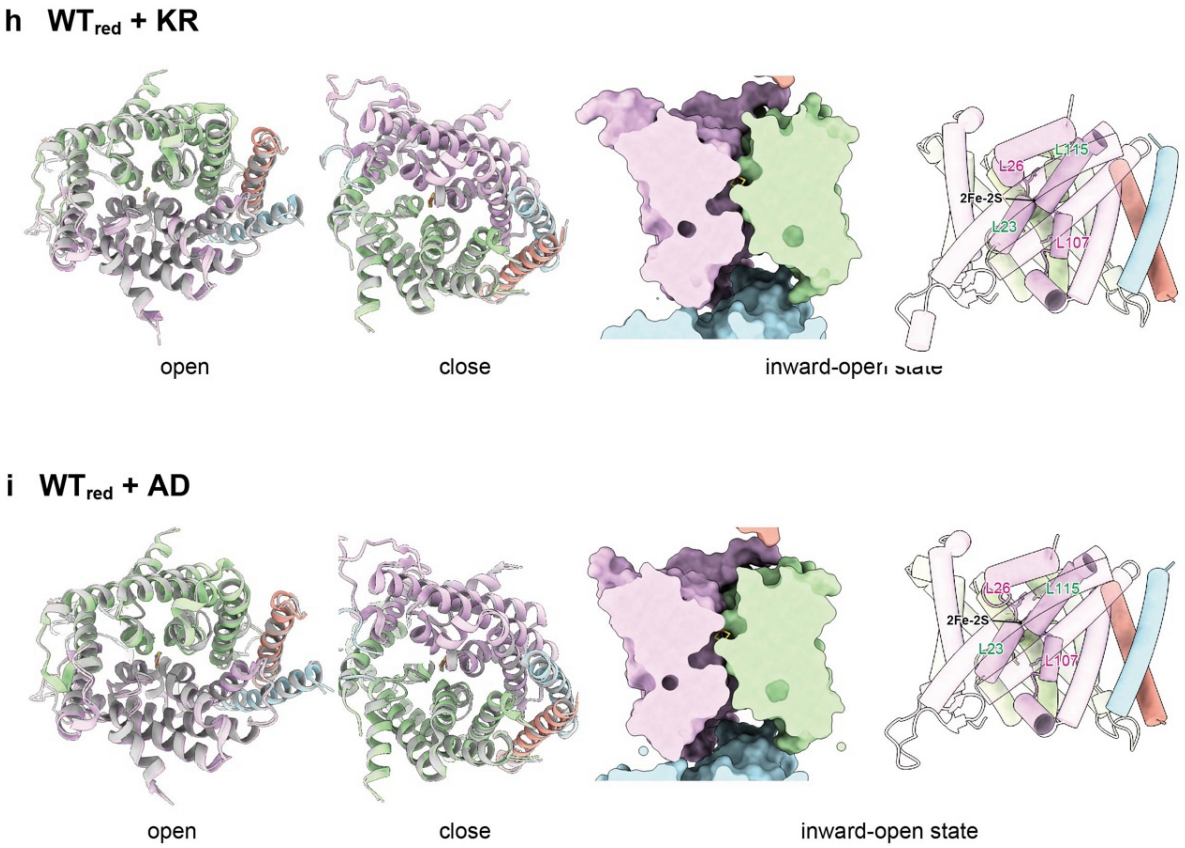

Extended Data Fig 2: TMHs shifts. The TMHs architecture of NqrCDEF. The *left* and *middle* panels show cytoplasmic views and periplasmic views, respectively. To help visualize the transition, the **WT_{ox}** structure is superimposed in *gray*. The *right* panel shows the sliced view. ***a***: **WT_{red}**, ***b***: "***up***" state from **WT_{red}/-Na^+**, ***c***: "***middle***" state from **WT_{red}/-Na^+**, ***d***: **NqrB-T236Y_{ox}**, ***e***: **NqrB-T236Y_{red}**, ***f***: **NqrC-T225Y_{ox}**, ***g***: **NqrC-T225Y_{red}**, ***h***: **WT_{red} + KR,** and ***i***: **WT_{red} + AD** are compared with **WT_{red},** respectively.

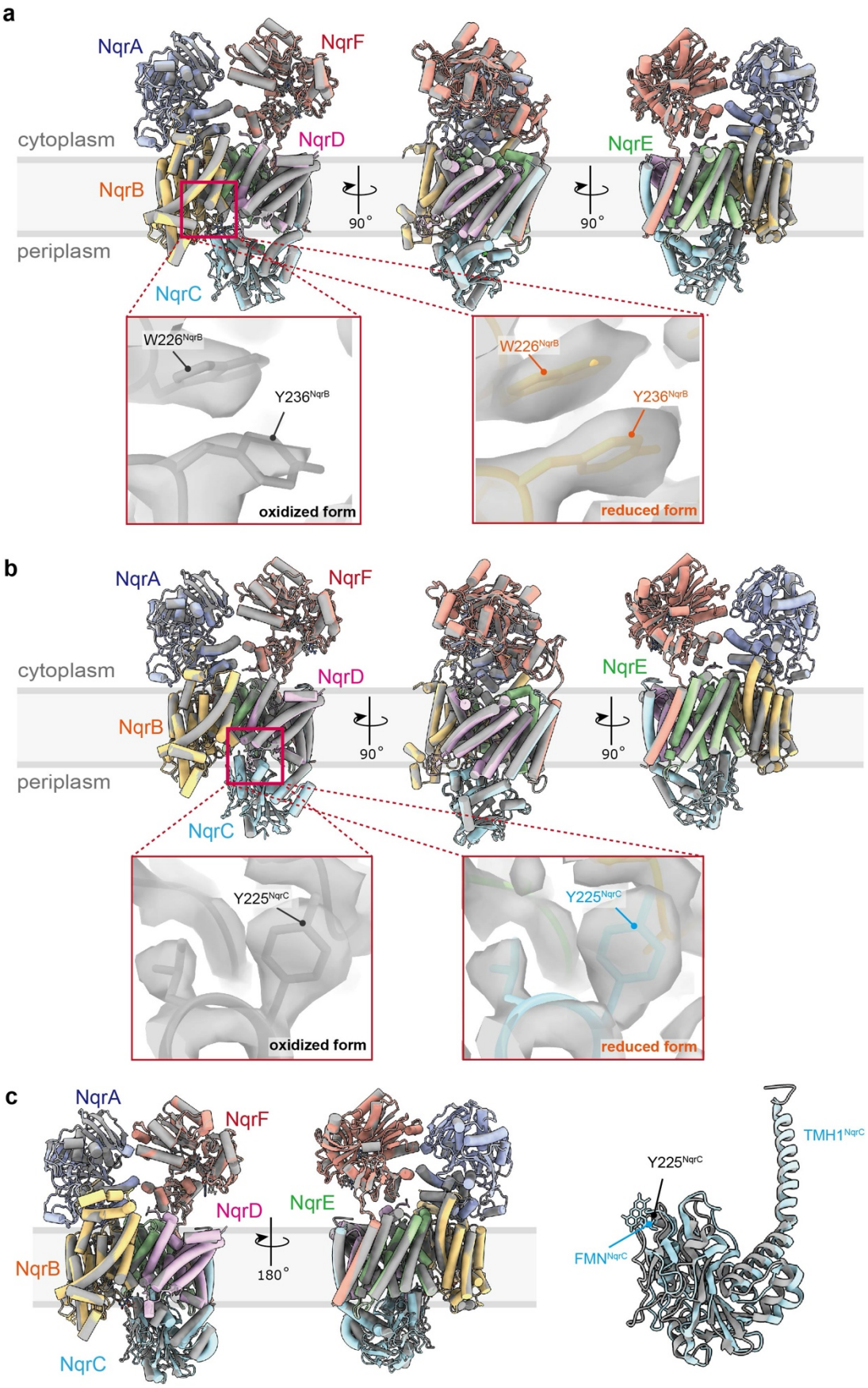

682
683
684 **Extended Data Fig. 3 (continued)**

685 **Extended Data Fig. 3: The architecture of FMN deletions.** ***a,*** Comparison of **NqrB-T236Y$_{ox}$** (*gray*)
686 and **NqrB-T236Y$_{red}$** (*color*). *Red square* shows the position of the point mutation. NqrB-Y236 in each
687 form is zoomed up with a density map in the bottom pictures. ***b,*** Comparison of **NqrC-T225Y$_{ox}$** (*gray*)
688 and **NqrC-T225Y$_{red}$** (*color*). *Red square* shows the position of the point mutation. NqrC-Y225 in each
689 form is zoomed up with a density map in the bottom pictures. ***c,*** Comparison of **NqrC-T225Y$_{red}$** (*gray*)
690 and the "*shifted*" state of **NqrB-G141A$_{red}$ + KR** (*color*). NqrC is picked up in *right* panel.
691
692

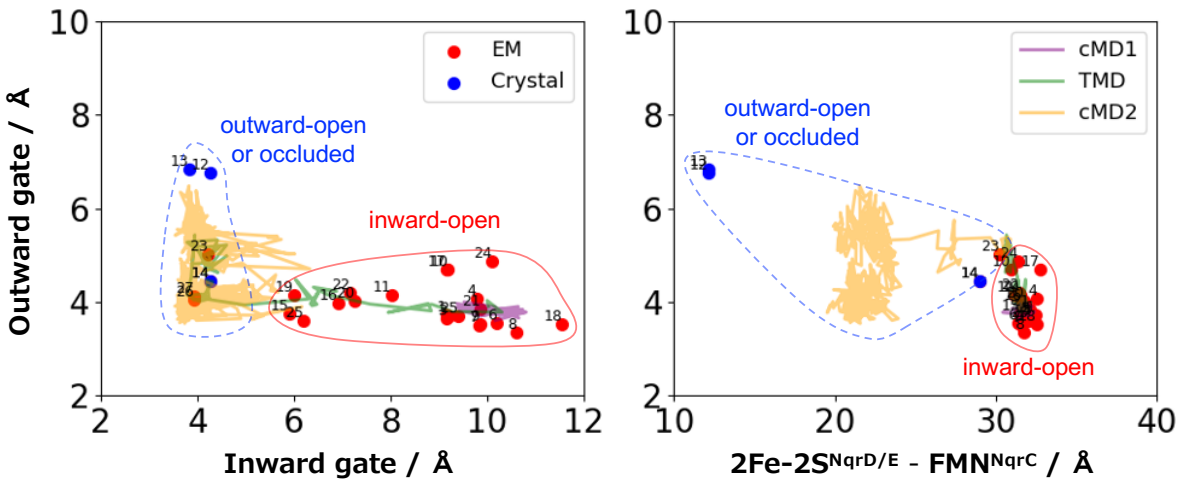

Index	Structure state: PDB ID
1	**WT_{ox} state1**: 7XK3
2	**WT_{ox} state2:** 7XK4
3	**WT_{ox} state3:** 7XK5
4	**WT_{ox} + AD-42:** 7XK6
5	**WT_{ox} + KR:** 7XK7
6	**WT_{ox}** : 8A1T
7	**WT_{red} + UQ2**: 8A1U
8	**WT_{ox} + UQ2**: 8A1V
9	**WT_{ox} + UQ1**: 8A1W
10	**WT_{ox} + DQA**: 8A1X
11	**WT_{ox} + HQNO**: 8A1Y
12	**WT_{ox}_1**: 8ACW (crystal)
13	**WT_{ox}_2**: 8ACY (crystal)
14	**WT_{ox}_3**: 8AD0 (crystal)

Index	Structure state: PDB ID
15	**WT_{red}**: 9UUU
16	**WT_{red}/-Na^+ (*up*)**: 9UD6
17	**WT_{red}/-Na^+ (*middle*)**: 9UD8
18	**WT_{red}/-Na^+ (*down*)**: 9UD9
19	**WT_{red} + KR**: 9UD5
20	**WT_{red} + AD-42**: 9UDG
21	**NqrB-G141A_{ox} + KR**: 9LRR
22	**NqrB-G141A_{red} + KR (*stable*)**: 9UDA
23	**NqrB-G141A_{red} + KR (*shifted*)**: 9UDF
24	**NqrB-T236Y_{oxd}**: 9UD3
25	**NqrB-T236Y_{red}**: 9UD4
26	**NqrC-T225Y_{ox}**: 9U5G
27	**NqrC-T225Y_{red}**: 9UD2

Extended Data Fig. 4: MD simulation trajectory compared to experimental structures. The inward gate and outward gate size are defined by the distances between L26^{NqrD} and L115^{NqrE}, and between L107^{NqrD} and L23^{NqrE}, respectively (Fig. 4a). The *left* panel shows a 2D plot of the inward gate and the outward gate distances. The *right* panel shows a 2D plot of the cofactors 2Fe-2S$^{NqrD/E}$ – FMN^{NqrC} distance and the outward gate distance. The numbers are from the bottom table.

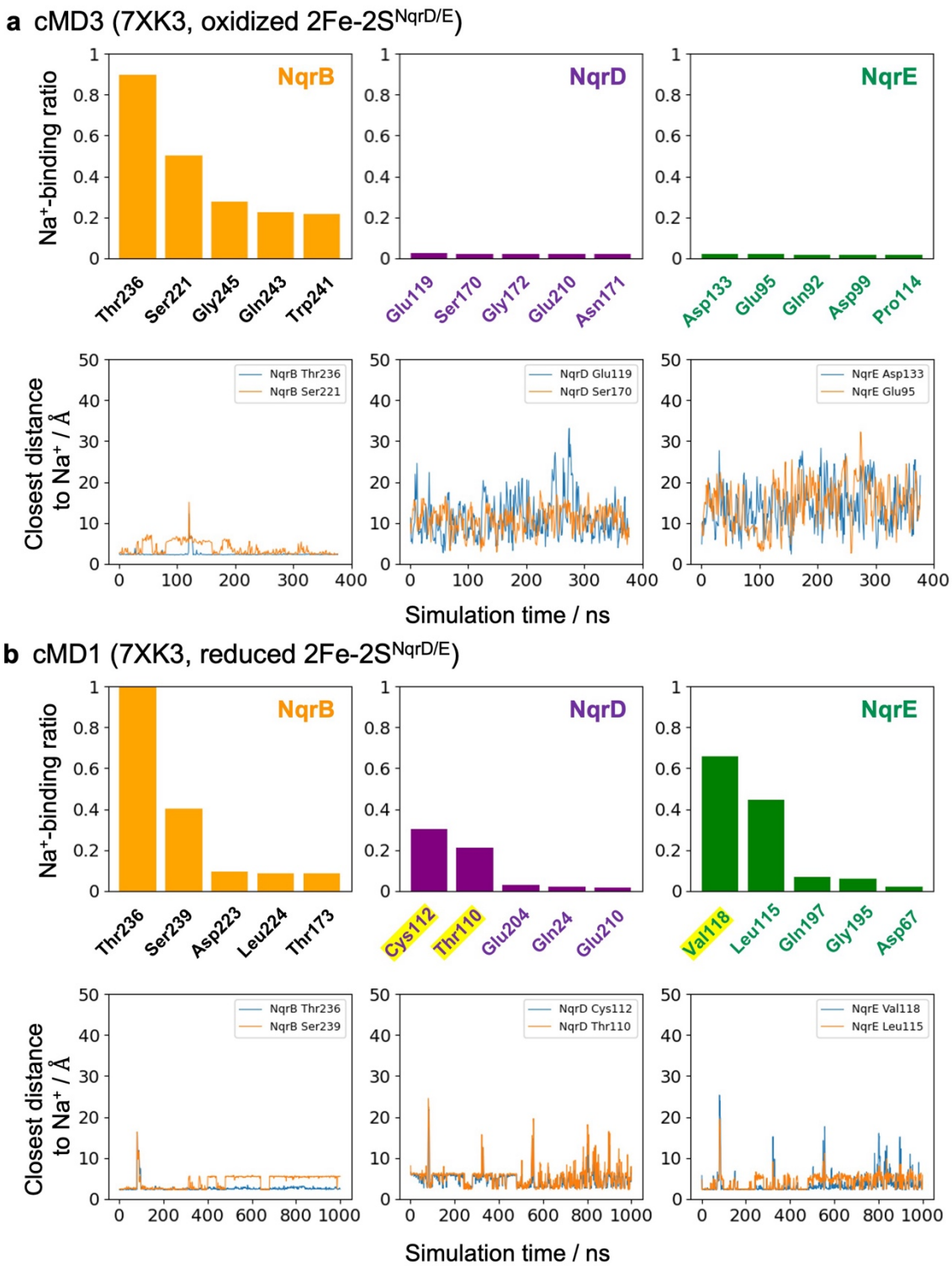

Extended Data Fig. 5 (continued)

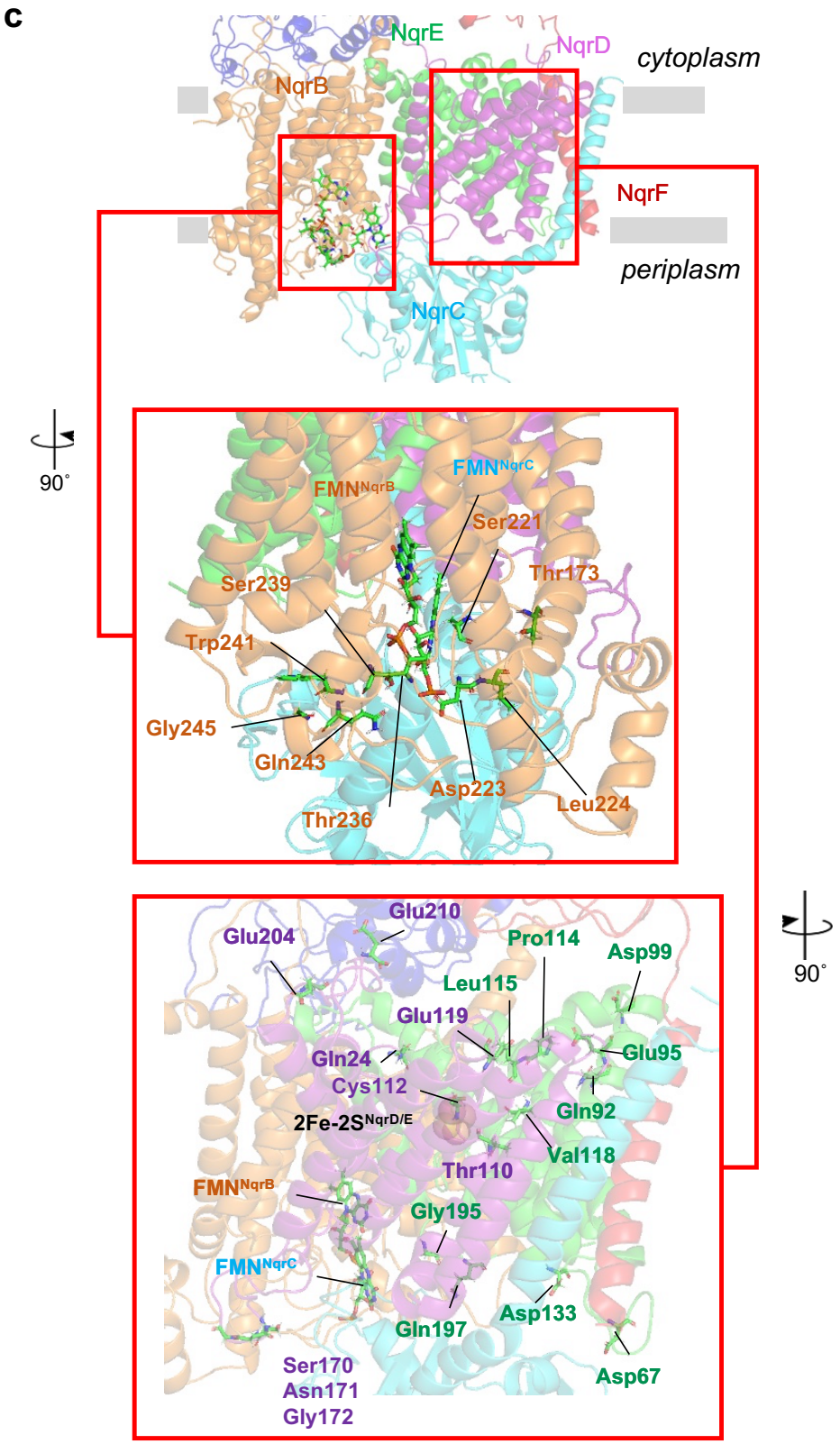

Extended Data Fig. 5 (continued)

Extended Data Fig. 5: Analysis of amino acid residues that are involved in Na^+ binding. a-b, Simulation is calculated at the scale of 400 ns. Contact ratio corresponds to the ratio of Na^+-binding frame to total frame. Residues showing > 0.01 of contact ratio and the > 3 Å of distance to were listed up. The *top* panels show the top five residues that have high Na^+ binding ratios for NqrB, NqrD, and NqrE, respectively. The Na^+ binding was defined through the distance being less than 3 Å. The *bottom* panels show the time course of the closest distances between the residues and Na^+. ***a,*** Analysis of MD simulation with oxidized cofactors (cMD3). ***b,*** Analysis of MD simulation with reduced 2Fe-2S$^{NqrD/E}$ cofactor (cMD1). ***c,*** The locations of amino acid residues in NqrB and NqrD/E that show a high Na^+ binding ratio in MD simulations. The *top* panel indicates the relative positions of the two regions containing amino acid residues with a high Na^+ binding ratio in TMHs. The *middle* panel shows the region around the FMN binding site in NqrB. The *bottom* panel shows the region of TMHs^{NqrCDEF} bundle.